Eur. Phys. J. C 4, 409–431 (1998)
DOI 10.1007/s100529800895

THE EUROPEAN PHYSICAL JOURNAL C

Measurement of the axial-vector τ spectral functions and determination of $\alpha_s(M_\tau^2)$ from hadronic τ decays

ALEPH Collaboration

R. Barate, D. Buskulic, D. Decamp, P. Ghez, C. Goy, J.-P. Lees, A. Lucotte, E. Merle, M.-N. Minard, J.-Y. Nief, B. Pietrzyk
Laboratoire de Physique des Particules (LAPP), IN^{2}P^3-CNRS, F-74019 Annecy-le-Vieux Cedex, France

R. Alemany, G. Boix, M.P. Casado, M. Chmeissani, J.M. Crespo, M. Delfino, E. Fernandez, M. Fernandez-Bosman, Ll. Garrido,[15] E. Graugès, A. Juste, M. Martinez, G. Merino, R. Miquel, Ll.M. Mir, I.C. Park, A. Pascual, J.A. Perlas, I. Riu, F. Sanchez
Institut de Física d'Altes Energies, Universitat Autònoma de Barcelona, E-08193 Bellaterra (Barcelona), Spain[7]

A. Colaleo, D. Creanza, M. de Palma, G. Gelao, G. Iaselli, G. Maggi, M. Maggi, S. Nuzzo, A. Ranieri, G. Raso, F. Ruggieri, G. Selvaggi, L. Silvestris, P. Tempesta, A. Tricomi,[3] G. Zito
Dipartimento di Fisica, INFN Sezione di Bari, I-70126 Bari, Italy

X. Huang, J. Lin, Q. Ouyang, T. Wang, Y. Xie, R. Xu, S. Xue, J. Zhang, L. Zhang, W. Zhao
Institute of High-Energy Physics, Academia Sinica, Beijing, The People's Republic of China[8]

D. Abbaneo, U. Becker, P. Bright-Thomas, D. Casper, M. Cattaneo, V. Ciulli, G. Dissertori, H. Drevermann, R.W. Forty, M. Frank, R. Hagelberg, J.B. Hansen, J. Harvey, P. Janot, B. Jost, I. Lehraus, P. Mato, A. Minten, L. Moneta,[21] A. Pacheco, J.-F. Pusztaszeri,[23] F. Ranjard, L. Rolandi, D. Rousseau, D. Schlatter, M. Schmitt,[25] O. Schneider, W. Tejessy, F. Teubert, I.R. Tomalin, H. Wachsmuth, A. Wagner[20]
European Laboratory for Particle Physics (CERN), CH-1211 Geneva 23, Switzerland

Z. Ajaltouni, F. Badaud, G. Chazelle, O. Deschamps, A. Falvard, C. Ferdi, P. Gay, C. Guicheney, P. Henrard, J. Jousset, B. Michel, S. Monteil, J-C. Montret, D. Pallin, P. Perret, F. Podlyski, J. Proriol, P. Rosnet
Laboratoire de Physique Corpusculaire, Université Blaise Pascal, IN^{2}P^3-CNRS, Clermont-Ferrand, F-63177 Aubière, France

J.D. Hansen, J.R. Hansen, P.H. Hansen, B.S. Nilsson, B. Rensch, A. Wäänänen
Niels Bohr Institute, DK-2100 Copenhagen, Denmark[9]

G. Daskalakis, A. Kyriakis, C. Markou, E. Simopoulou, I. Siotis, A. Vayaki
Nuclear Research Center Demokritos (NRCD), GR-15310 Attiki, Greece

A. Blondel, G. Bonneaud, J.-C. Brient, P. Bourdon, A. Rougé, M. Rumpf, A. Valassi,[6] M. Verderi, H. Videau
Laboratoire de Physique Nucléaire et des Hautes Energies, Ecole Polytechnique, IN^{2}P^3-CNRS, F- 91128 Palaiseau Cedex, France

E. Focardi, G. Parrini, K. Zachariadou
Dipartimento di Fisica, Università di Firenze, INFN Sezione di Firenze, I-50125 Firenze, Italy

M. Corden, C. Georgiopoulos, D.E. Jaffe
Supercomputer Computations Research Institute, Florida State University, Tallahassee, FL 32306-4052, USA [13,14]

A. Antonelli, G. Bencivenni, G. Bologna,[4] F. Bossi, P. Campana, G. Capon, F. Cerutti, V. Chiarella, G. Felici, P. Laurelli, G. Mannocchi,[5] F. Murtas, G.P. Murtas, L. Passalacqua, M. Pepe-Altarelli
Laboratori Nazionali dell'INFN (LNF-INFN), I-00044 Frascati, Italy

L. Curtis, A.W. Halley, J.G. Lynch, P. Negus, V. O'Shea, C. Raine, J.M. Scarr, K. Smith, P. Teixeira-Dias, A.S. Thompson, E. Thomson
Department of Physics and Astronomy, University of Glasgow, Glasgow G12 8QQ,United Kingdom[10]

O. Buchmüller, S. Dhamotharan, C. Geweniger, G. Graefe, P. Hanke, G. Hansper, V. Hepp, E.E. Kluge, A. Putzer, J. Sommer, K. Tittel, S. Werner, M. Wunsch
Institut für Hochenergiephysik, Universität Heidelberg, D-69120 Heidelberg, Germany[16]

R. Beuselinck, D.M. Binnie, W. Cameron, P.J. Dornan,[2] M. Girone, S. Goodsir, E.B. Martin, N. Marinelli, A. Moutoussi, J. Nash, J.K. Sedgbeer, P. Spagnolo, M.D. Williams
Department of Physics, Imperial College, London SW7 2BZ, United Kingdom[10]

V.M. Ghete, P. Girtler, E. Kneringer, D. Kuhn, G. Rudolph
Institut für Experimentalphysik, Universität Innsbruck, A-6020 Innsbruck, Austria[18]

A.P. Betteridge, C.K. Bowdery, P.G. Buck, P. Colrain, G. Crawford, A.J. Finch, F. Foster, G. Hughes, R.W.L. Jones, M.I. Williams
Department of Physics, University of Lancaster, Lancaster LA1 4YB, United Kingdom[10]

I. Giehl, A.M. Greene, C. Hoffmann, K. Jakobs, K. Kleinknecht, G. Quast, B. Renk, E. Rohne, H.-G. Sander, P. van Gemmeren, C. Zeitnitz
Institut für Physik, Universität Mainz, D-55099 Mainz, Germany[16]

J.J. Aubert, C. Benchouk, A. Bonissent, G. Bujosa, J. Carr,[2] P. Coyle, F. Etienne, O. Leroy, F. Motsch, P. Payre, M. Talby, A. Sadouki, M. Thulasidas, K. Trabelsi
Centre de Physique des Particules, Faculté des Sciences de Luminy, IN^2P^3-CNRS, F-13288 Marseille, France

M. Aleppo, M. Antonelli, F. Ragusa
Dipartimento di Fisica, Università di Milano e INFN Sezione di Milano, I-20133 Milano, Italy

R. Berlich, W. Blum, V. Büscher, H. Dietl, G. Ganis, H. Kroha, G. Lütjens, C. Mannert, W. Männer, H.-G. Moser, S. Schael, R. Settles, H. Seywerd, H. Stenzel, W. Wiedenmann, G. Wolf
Max-Planck-Institut für Physik, Werner-Heisenberg-Institut, D-80805 München, Germany[p]

J. Boucrot, O. Callot, S. Chen, A. Cordier, M. Davier, L. Duflot, J.-F. Grivaz, Ph. Heusse, A. Höcker, A. Jacholkowska, D.W. Kim,[12] F. Le Diberder, J. Lefrançois, A.-M. Lutz, M.-H. Schune, E. Tournefier, J.-J. Veillet, I. Videau, D. Zerwas
Laboratoire de l'Accélérateur Linéaire, Université de Paris-Sud, IN^2P^3-CNRS, F-91405 Orsay Cedex, France

P. Azzurri, G. Bagliesi,[2] G. Batignani, S. Bettarini, T. Boccali, C. Bozzi, G. Calderini, M. Carpinelli, M.A. Ciocci, R. Dell'Orso, R. Fantechi, I. Ferrante, L. Foà,[1] F. Forti, A. Giassi, M.A. Giorgi, A. Gregorio, F. Ligabue, A. Lusiani, P.S. Marrocchesi, A. Messineo, F. Palla, G. Rizzo, G. Sanguinetti, A. Sciabà, R. Tenchini, G. Tonelli,[19] C. Vannini, A. Venturi, P.G. Verdini
Dipartimento di Fisica dell'Università, INFN Sezione di Pisa, e Scuola Normale Superiore, I-56010 Pisa, Italy

G.A. Blair, L.M. Bryant, J.T. Chambers, M.G. Green, T. Medcalf, P. Perrodo, J.A. Strong, J.H. von Wimmersperg-Toeller
Department of Physics, Royal Holloway & Bedford New College, University of London, Surrey TW20 OEX, United Kingdom[10]

D.R. Botterill, R.W. Clifft, T.R. Edgecock, S. Haywood, P.R. Norton, J.C. Thompson, A.E. Wright
Particle Physics Dept., Rutherford Appleton Laboratory, Chilton, Didcot, Oxon OX11 OQX, United Kingdom[10]

B. Bloch-Devaux, P. Colas, S. Emery, W. Kozanecki, E. Lançon,[2] M.-C. Lemaire, E. Locci, P. Perez, J. Rander, J.-F. Renardy, A. Roussarie, J.-P. Schuller, J. Schwindling, A. Trabelsi, B. Vallage
CEA, DAPNIA/Service de Physique des Particules, CE-Saclay, F-91191 Gif-sur-Yvette Cedex, France[17]

S.N. Black, J.H. Dann, R.P. Johnson, H.Y. Kim, N. Konstantinidis, A.M. Litke, M.A. McNeil, G. Taylor
Institute for Particle Physics, University of California at Santa Cruz, Santa Cruz, CA 95064, USA[22]

C.N. Booth, C.A.J. Brew, S. Cartwright, F. Combley, M.S. Kelly, M. Lehto, J. Reeve, L.F. Thompson
Department of Physics, University of Sheffield, Sheffield S3 7RH, United Kingdom[10]

K. Affholderbach, A. Böhrer, S. Brandt, G. Cowan, C. Grupen, P. Saraiva, L. Smolik, F. Stephan
Fachbereich Physik, Universität Siegen, D-57068 Siegen, Germany[16]

M. Apollonio, L. Bosisio, R. Della Marina, G. Giannini, B. Gobbo, G. Musolino
Dipartimento di Fisica, Università di Trieste e INFN Sezione di Trieste, I-34127 Trieste, Italy

J. Rothberg, S. Wasserbaech
Experimental Elementary Particle Physics, University of Washington, WA 98195 Seattle, USA

S.R. Armstrong, E. Charles, P. Elmer, D.P.S. Ferguson, Y. Gao, S. González, T.C. Greening, O.J. Hayes, H. Hu, S. Jin, P.A. McNamara III, J.M. Nachtman,[24] J. Nielsen, W. Orejudos, Y.B. Pan, Y. Saadi, I.J. Scott, J. Walsh, Sau Lan Wu, X. Wu, G. Zobernig
Department of Physics, University of Wisconsin, Madison, WI 53706, USA[11]

Received: 26 January 1998 / Published online: 15 June 1998

Abstract. An analysis based on 124 000 selected τ pairs recorded by the ALEPH detector at LEP provides the vector (V) and axial-vector (A) spectral functions of hadronic τ decays together with their total widths. This allows the evaluation of finite energy chiral sum rules that are weighted integrals over the $(V-A)$ spectral functions. In addition, a precise measurement of α_s along with a determination of non-perturbative contributions at the τ mass scale is performed. The experimentally and theoretically most robust determination of $\alpha_s(M_\tau^2)$ is obtained from the $(V+A)$ fit that yields $\alpha_s(M_\tau^2) = 0.334 \pm 0.022$ giving $\alpha_s(M_Z^2) = 0.1202 \pm 0.0027$ after the extrapolation to the mass of the Z boson. The approach of the Operator Product Expansion (OPE) is tested experimentally studying the evolution of the τ hadronic widths to masses smaller than the τ mass.

1 Introduction

Observables that give access to the inner structure of hadronic τ decays are the so-called *spectral functions*. These are the invariant mass spectra of the hadronic final states, normalized to their branching ratios and corrected for the τ decay kinematics. As parity is maximally violated in τ decays, its spectral functions have both *vector* and *axial-vector* contributions. The measurement of the non-strange τ vector (axial-vector) current spectral functions requires the selection and identification of hadronic τ decay modes with a defined G-parity $\mathrm{G} = +1$ ($\mathrm{G} = -1$), i.e., channels with an even (odd) number of neutral *or* charged pions. Any difference in the normalization (branching ratios) or the shape between vector and axial-vector spectral functions is necessarily generated by nonperturbative QCD as, e.g., long distance resonance phenomena. The most prominent are the well-known $\rho(770)$ vector and $a_1(1260)$ axial-vector mesons. For nonperturbative effects to be studied, a clear experimental separation of the hadronic τ decay channels into vector and axial-vector states is necessary. Experimental and conceptual problems concerning this separation have already been discussed in

[1] Now at CERN, 1211 Geneva 23, Switzerland.
[2] Also at CERN, 1211 Geneva 23, Switzerland.
[3] Also at Dipartimento di Fisica, INFN, Sezione di Catania, Catania, Italy.
[4] Also Istituto di Fisica Generale, Università di Torino, Torino, Italy.
[5] Also Istituto di Cosmo-Geofisica del C.N.R., Torino, Italy.
[6] Supported by the Commission of the European Communities, contract ERBCHBICT941234.
[7] Supported by CICYT, Spain.
[8] Supported by the National Science Foundation of China.
[9] Supported by the Danish Natural Science Research Council.
[10] Supported by the UK Particle Physics and Astronomy Research Council.
[11] Supported by the US Department of Energy, grant DE-FG0295-ER40896.
[12] Permanent address: Kangnung National University, Kangnung, Korea.
[13] Supported by the US Department of Energy, contract DE-FG05-92ER40742.
[14] Supported by the US Department of Energy, contract DE-FC05-85ER250000.
[15] Permanent address: Universitat de Barcelona, 08208 Barcelona, Spain.
[16] Supported by the Bundesministerium für Bildung, Wissenschaft, Forschung und Technologie, Germany.
[17] Supported by the Direction des Sciences de la Matière, C.E.A.
[18] Supported by Fonds zur Förderung der wissenschaftlichen Forschung, Austria.
[19] Also at Istituto di Matematica e Fisica, Università di Sassari, Sassari, Italy.
[20] Now at Schweizerischer Bankverein, Basel, Switzerland.
[21] Now at University of Geneva, 1211 Geneva 4, Switzerland.
[22] Supported by the US Department of Energy, grant DE-FG03-92ER40689.
[23] Now at School of Operations Research and Industrial Engineering, Cornell University, Ithaca, NY 14853-3801, USA
[24] Now at University of California at Los Angeles (UCLA), Los Angeles, CA 90024, USA
[25] Now at Harvard University, Cambridge, MA 02138, USA

a previous ALEPH publication of the vector spectral functions and related applications [1].

In this article, the non-strange axial-vector spectral function is measured and, together with the previously measured vector spectral function, is used to determine α_s at the scale of the τ mass and to test the underlying phenomenological approach to low energy QCD. A determination of $\alpha_s(M_\tau^2)$ was carried out for the first time by ALEPH [2] and CLEO [3].

At the quark-parton level and ignoring quark masses, the branching ratio $B(\tau \to q'\bar{q}\,\nu_\tau)$ is predicted to be 3/5. Because of gluon radiation and loop effects, the hadronic branching ratio is increased and its measured value can thus be used to determine α_s. The *Operator Product Expansion* (OPE) [4] enables a theoretical prediction of the inclusive vector/axial-vector τ hadronic width and spectral moments to be made as a function of both α_s and nonperturbative phenomenological operators [5]. These operators are part of a power series in $1/M_\tau$ and can be determined experimentally [6]. In this article, the consistency of the OPE ansatz and the stability of the α_s measurement are studied by comparing data with the theoretical prediction of the τ hadronic width evolved to masses smaller than the τ mass. Different theoretical approaches to the perturbative prediction are investigated.

Tests of Quantum Chromodynamics and the measurement of the strong coupling constant α_s at the τ mass scale have been the subject of a large number of publications (see, e.g., [5–10]).

The paper is organized as follows. After the definition of the τ vector and axial-vector spectral functions, a brief introduction of the ALEPH experiment is given and the measurement procedure is outlined. The vector and axial-vector spectral functions are exploited in order to test chiral sum rules. Then $\alpha_s(M_\tau^2)$ is determined and the spectral moments are used to access the nonperturbative power corrections to the τ hadronic widths. Finally a test of the OPE approach is performed with an analysis of the evolution of the τ hadronic widths as a function of a varying "τ" mass $s_0 < M_\tau^2$.

2 Spectral functions

The spectral function v_1 (a_1, a_0), where the subscript refers to the spin J of the hadronic system, is here defined for a non-strange vector (axial-vector) hadronic τ decay channel $V^-\,\nu_\tau$ ($A^-\,\nu_\tau$). Subsequently throughout this article the notation V/A will be used to mean vector and axial-vector, *respectively*. The spectral function is obtained by dividing the normalized invariant mass-squared distribution $(1/N_{V/A})(dN_{V/A}/ds)$ for a given hadronic mass $\sqrt{s}$ by the appropriate kinematic factor

$$v_1(s)/a_1(s) \equiv \frac{M_\tau^2}{6\,|V_{ud}|^2\,S_{\rm EW}}\,\frac{B(\tau^- \to V^-/A^-\,\nu_\tau)}{B(\tau^- \to e^-\,\bar{\nu}_e\nu_\tau)} \times \frac{dN_{V/A}}{N_{V/A}\,ds}\,\left[\left(1-\frac{s}{M_\tau^2}\right)^2\left(1+\frac{2s}{M_\tau^2}\right)\right]^{-1}, \quad (1)$$

$$a_0(s) \equiv \frac{M_\tau^2}{6\,|V_{ud}|^2\,S_{\rm EW}}\,\frac{B(\tau^- \to \pi^-\,\nu_\tau)}{B(\tau^- \to e^-\,\bar{\nu}_e\nu_\tau)}\,\frac{dN_A}{N_A\,ds} \times \left(1-\frac{s}{M_\tau^2}\right)^{-2}, \quad (2)$$

where $|V_{ud}| = 0.9752 \pm 0.0007$ [11] denotes the CKM weak mixing matrix element and $S_{\rm EW} = 1.0194 \pm 0.0040$ accounts for electroweak radiative corrections [12] (see also the discussion in [16]). Due to the conserved vector current, there is no $J = 0$ contribution to the vector spectral function, while the only contribution to a_0 is assumed to be from the pion pole. It is connected via PCAC to the pion decay constant, $a_{0,\,\pi}(s) = 4\pi^2 f_\pi^2\,\delta(s - m_\pi^2)$. The spectral functions are normalized by the ratio of the vector/axial-vector branching fraction $B(\tau^- \to V^-/A^-\,\nu_\tau)$ to the branching fraction of the massless leptonic, i.e., electron, channel

$$B(\tau^- \to e^-\,\bar{\nu}_e\nu_\tau) = (17.794 \pm 0.045)\%\,, \quad (3)$$

where the value includes the improvement in accuracy provided by the universality assumption of leptonic currents together with the measurements $B(\tau^- \to e^-\,\bar{\nu}_e\nu_\tau) = (17.83 \pm 0.08)\%$ [11], $B(\tau^- \to \mu^-\,\bar{\nu}_\mu\nu_\tau) = (17.30 \pm 0.09)\%$ [13,14] and the τ lifetime $\tau_\tau = (290.0 \pm 1.2)$ fs [15]. The τ mass of $M_\tau = 1776.96^{+0.31}_{-0.27}$ MeV/c^2 is taken from the BES measurement [17].

Using unitarity and analyticity, the spectral functions of hadronic τ decays are connected to the imaginary part of the two-point correlation (or hadronic vacuum polarization) functions [5,8] $\Pi^{\mu\nu}_{ij,U}(q) \equiv i\int d^4x\, e^{iqx}\,\langle 0|T(U^\mu_{ij}(x)U^\nu_{ij}(0)^\dagger)|0\rangle = (-g^{\mu\nu}q^2 + q^\mu q^\nu)\,\Pi^{(1)}_{ij,U}(q^2) + q^\mu q^\nu\,\Pi^{(0)}_{ij,U}(q^2)$ of vector ($U^\mu_{ij} \equiv V^\mu_{ij} = \bar{q}_j\gamma^\mu q_i$) or axial-vector ($U^\mu_{ij} \equiv A^\mu_{ij} = \bar{q}_j\gamma^\mu\gamma_5 q_i$) colour-singlet quark currents in corresponding quantum states and for time-like momenta-squared $q^2 > 0$. Lorentz decomposition is used to separate the correlation function into its $J = 1$ and $J = 0$ parts. Thus, using the definition (1), one identifies for non-strange quark currents

$$\mathrm{Im}\,\Pi^{(1)}_{\bar{u}d,V/A}(s) = \frac{1}{2\pi}v_1/a_1(s)\,,$$
$$\mathrm{Im}\,\Pi^{(0)}_{\bar{u}d,A}(s) = \frac{1}{2\pi}a_0(s)\,, \quad (4)$$

which provide the basis for comparing theory with data.

3 The ALEPH detector

The ALEPH detector provides both tracking and calorimetric information over almost the full solid angle. The features relevant for this analysis are briefly mentioned here, while a detailed description of its components and performance can be found in [18,19].

The momentum of charged particles is reconstructed using the information given by three tracking devices immersed in a 1.5 T axial magnetic field: a double-sided silicon microstrip vertex detector, an eight-layer axial wire

chamber, and a large time projection chamber (TPC) providing up to 21 space points for tracks of charged particles and up to 338 measurements of the ionization loss (dE/dx). The transverse momentum resolution achieved is $\Delta(1/p_{\mathrm{T}}) \simeq 0.6 \times 10^{-3}$ (GeV/c)$^{-1}$.

The electromagnetic calorimeter (ECAL), located inside the magnetic coil, is formed of a barrel surrounding the TPC, closed at each end by an endcap. It consists of 45 layers of a total thickness of 22 radiation lengths. The energy and position of a shower is read out using cathode pads with dimensions 3×3 cm^2, arranged to form towers pointing to the interaction zone; each tower is read out in three segments in depth corresponding to 4, 9, and 9 radiation lengths. The energy resolution is $\Delta E/E \simeq 18\%/\sqrt{E\ (\mathrm{GeV})} + 0.9\%$. There are 74 000 such towers, with an average granularity of $0.9^\circ \times 0.9^\circ$. The inactive zones ("cracks") between the ECAL modules represent 2% of the total solid angle in the barrel and 6% in the endcaps. The fine granularity and the longitudinal segmentation of the calorimeter play an important role in the photon and neutral pion reconstruction, and in the identification of fake photons produced by hadronic interactions of charged hadrons or by signal fluctuations from electromagnetic showers.

The hadron calorimeter (HCAL) has 23 layers of iron absorber each 5 cm thick interleaved with limited streamer tubes 9×9 mm^2 in cross section. The tower read-out is built from pads with an angular size of $3.7^\circ \times 3.7^\circ$. Strips running along the tubes provide a digital readout giving a two-dimensional view of the development of hadronic showers and muon trajectories.

Finally, muons are also detected by two double layers of streamer tubes outside the HCAL.

The trigger efficiency is measured to be better than 99.99% for the selection cuts of this analysis.

Tau pair events produced at the Z mass peak are simulated using the standard Monte Carlo program KORALZ [20–22] and passed through a full detector simulation based on GEANT [23]. Electromagnetic showers are simulated according to parametrizations obtained from test beam data [18]. Several tests and corrections of the detector simulation have been carried out within the scope of this analysis to assure its reliability and to estimate systematic uncertainties [24].

4 The measurement procedure

The measurement of the spectral functions defined in (1) requires the determination of the physical invariant mass-squared distribution. The details of the analysis are reported in [1]. In the following, a brief outline of the important steps of the measurement procedure is given:

Tau pairs originating from Z^0 decays are detected utilizing their characteristic collinear jet signature and the low multiplicity of their decays. Using the data from 1991–1994, a total of 124 358 τ pairs is selected corresponding to a detection efficiency of $(78.84 \pm 0.13)\%$. The overall non-τ background contribution in the hadronic modes amounts to $(0.6 \pm 0.2)\%$. Details about the ALEPH τ pair selection are given in [25,13,26].

Charged particles (electrons, muons and hadrons) are identified employing a maximum likelihood method to combine different and essentially uncorrelated information measured for each individual track. Discriminating variables used are the specific ionization loss, dE/dx, the transverse and longitudinal shower profile of the energy deposition in the ECAL, the average width of hadronic showers and the number of hits in the HCAL and the muon chambers. The procedure and the discriminating variables used in this analysis are described in [27,13]. The momentum calibration of charged tracks is performed using $e^+e^- \to \mu^+\mu^-$ events and using the invariant mass measurement of well-known, narrow resonances at low and intermediate energies. The resulting calibration uncertainty amounts to less than 0.1%.

Photons are reconstructed by collecting associated energetic electromagnetic calorimeter (ECAL) towers, forming a cluster. To distinguish genuine photons from fake photons a likelihood method is applied using ECAL information, e.g., the fraction of energy in the ECAL stacks, the transverse size of the shower or the distance between the barycentre of the cluster and the closest charged track. The energy calibration is performed using electrons originating from Bhabha, τ and two-photon events. A relative calibration uncertainty of about 1.5% at low energy, 1% at intermediate energies and 0.5% at high energy is obtained.

The **π^0 finder** uses a π^0-mass constraint fit to attribute two reconstructed photons to the corresponding π^0 decay. At higher π^0 energy, the opening angle between the boosted photons tends to become smaller than the calorimeter resolution so that the two electromagnetic showers are often merged in one cluster. The transverse energy distribution in the ECAL nevertheless allows the computation of energy-weighted moments providing a measure of the two-photon invariant mass. Remaining photons are considered as originating from a π^0 where the second photon has been lost.

The **classification** of the inclusive hadronic τ decay channels is performed according to [26] on the basis of the number of reconstructed charged and neutral pions. The exclusive channels listed in Table 1 are obtained by subtracting the τ and non-τ background and the strange contribution from the inclusive measurements using the Monte Carlo simulation. In order to extract the physical invariant mass spectra from the measured ones they need to be unfolded from the effects of measurement distortion.

The **unfolding method** used here is based on the regularized inversion of the detector response matrix, obtained from the Monte Carlo simulation, using the *Singular Value Decomposition* technique. The regularization function applied minimizes the average curvature of the distribution. The optimal choice of the regularization strength is found by means of the Monte Carlo simulation where the true distribution is known. Details about the method are published in [28].

4.1 Systematic errors

The study of systematic errors affecting the measurement is subdivided into several classes according to their origin, viz., the photon and π^0 reconstruction, the charged track measurement, the unfolding procedure and additional sources. Since an unfolding procedure based upon a detector response matrix from the Monte Carlo simulation is used, the reliability of the simulation has to be subjected to detailed studies [1,26].

In order to check the photon reconstruction in the ECAL, the influence of calibration and resolution uncertainties is studied as well as possible variations on the reference distributions of a likelihood procedure used to veto fake photon candidates. The energy distribution of fake photons and the photon detection efficiency, both at threshold energies ($E_\gamma^{\rm thresh} = 300$ MeV) and in the neighbourhood of charged tracks, are also investigated.

Similarly, the effects of momentum calibration and resolution uncertainties in the reconstruction of charged tracks are checked, accompanied by tests of the reconstruction efficiency of highly collimated multi-prong events, and the simulation of secondary nuclear interactions.

In addition, systematic errors introduced by the unfolding procedure are tested by comparing known, true distributions to their corresponding unfolded ones and by varying the regularization conditions.

Finally, systematic errors due to the limited Monte Carlo statistics and to uncertainties in the branching ratios are added.

In order to illustrate the importance of these systematic uncertainties, one may perform an integration over the spectral functions with some given kernel, characteristic of a given physical problem. The integration error is then obtained by Gaussian error propagation taking into account the correlations. Using moderately s-dependent integration kernels, the integration error is dominated by normalization uncertainties, *i.e.*, the errors on the contributing τ branching ratios. However, the error on an integration with a strongly s-dependent weighting kernel enhancing the low energy parts of the spectral functions is dominated by systematics (mainly due to the fake photon rejection and the photon efficiency correction at threshold), while the central energy region ($0.6-1.4$ GeV$^2/c^4$) is statistically limited. When enhancing the higher part of the spectrum, the integration error is equally dominated by uncertainties due to the unfolding process, and by limited data and Monte Carlo statistics.

4.2 Invariant mass spectra and spectral functions

The above measurement procedure provides the physical invariant mass spectra of the measured τ decay modes including their bin-to-bin covariance matrices obtained, after the unfolding of the spectra, from the statistical errors and the study of systematic uncertainties.

The exclusive vector and axial-vector τ decay channels are listed in Table 1. Unless otherwise specified, their branching ratios are taken from ALEPH publications [26, 29] applying small corrections taking into account new ALEPH results on branching fractions of τ decay modes involving kaons [30]: the latter are listed in the Appendix. In some cases, additional information is taken from the Particle Data Group [11] as described in [1]. The individual fractions have been refitted so that the sum of all hadronic and leptonic branching ratios adds up to 100%, where the latter are derived from (3) assuming universality of the lepton couplings. This normalization slightly modifies the values given in the above references. The branching ratios of the subsequent meson decays are taken from [11]. The two-, four- and, in part, the six-pion modes are exclusively reconstructed. Special care is taken with isospin-violating ω and η decays, and with kaon pair production.

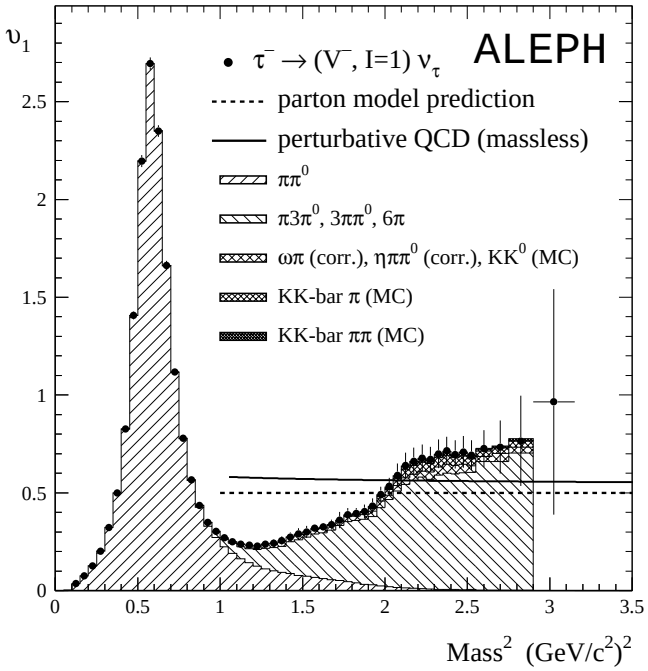

Fig. 1. Total vector spectral function. The shaded areas indicate the contributions from the exclusive τ vector channels, where the shapes of the contributions labeled "MC" are taken from the Monte Carlo simulation. The lines show the predictions from the naive parton model and from massless perturbative QCD using $\alpha_s(M_Z^2) = 0.120$

4.3 The total vector spectral function

The complete inclusive τ vector spectral function and its contributions are shown in Fig. 1. The dashed line depicts the naive parton model prediction while the massless QCD prediction [37] using $\alpha_s(M_Z^2) = 0.120$ (solid line) lies roughly 14% higher at M_τ^2. One observes that at $s \sim M_\tau^2$ the inclusive τ vector spectral function is larger than the QCD prediction, i.e., the asymptotic region is not reached.

The two- and four-pion final states are measured exclusively, while the six-pion state is only partly measured. The total six-pion branching ratio has been determined

Table 1. Vector and axial-vector hadronic τ decay modes with their contributing branching fractions. The branching ratios shown are refitted so that the compilation of all τ decay channels sums up to one. Further information about the branching ratios involving kaons used is given in the Appendix

Vector	BR (in %)	Axial-Vector	BR (in %)
$\pi^-\pi^0\,\nu_\tau$	25.34 ± 0.19	$\pi^-\,\nu_\tau$	11.23 ± 0.16
$\pi^-3\pi^0\,\nu_\tau$	1.18 ± 0.14	$\pi^-2\pi^0\,\nu_\tau$	9.23 ± 0.17
$2\pi^-\pi^+\pi^0\,\nu_\tau$	2.42 ± 0.09	$2\pi^-\pi^+\,\nu_\tau$	9.15 ± 0.15
$\pi^-5\pi^0\,\nu_\tau$		$\pi^-4\pi^0\,\nu_\tau$	$0.03 \pm 0.03^{(1)}$
$2\pi^-\pi^+3\pi^0\,\nu_\tau$	$0.04 \pm 0.02^{(1)}$	$2\pi^-\pi^+2\pi^0\,\nu_\tau$	0.10 ± 0.02
$3\pi^-2\pi^+\pi^0\,\nu_\tau$		$3\pi^-2\pi^+\,\nu_\tau$	0.07 ± 0.01
$\omega\,\pi^-\,\nu_\tau{}^{(2)}$	1.93 ± 0.10	$\omega\,\pi^-\pi^0\,\nu_\tau{}^{(2)}$	0.39 ± 0.11
$\eta\,\pi^-\pi^0\,\nu_\tau{}^{(3)}$	0.17 ± 0.03	$\eta\,2\pi^-\pi^+\,\nu_\tau$	0.04 ± 0.01
–	–	$\eta\,\pi^-2\pi^0\,\nu_\tau$	0.02 ± 0.01
$K^-K^0\,\nu_\tau$	0.19 ± 0.04	–	–
$K^-K^+\pi^-\,\nu_\tau$	0.08 ± 0.08	$K^-K^+\pi^-\,\nu_\tau$	0.08 ± 0.08
$K^0\bar{K}^0\pi^-\,\nu_\tau$	$0.08 \pm 0.08^{(1)}$	$K^0\bar{K}^0\pi^-\,\nu_\tau$	0.08 ± 0.08
$K^-K^0\pi^0\,\nu_\tau$	0.05 ± 0.05	$KK^0\pi^0\,\nu_\tau$	0.05 ± 0.05
$K\bar{K}\pi\pi\,\nu_\tau$	$0.08 \pm 0.08^{(1)}$	$K\bar{K}\pi\pi\,\nu_\tau$	$0.08 \pm 0.08^{(1)}$
Total Vector	31.58 ± 0.29	Total Axial-Vector	30.56 ± 0.30

[1] The branching ratio is obtained using constraints from isospin symmetry (see text and [1])
[2] Through $\omega \to \pi^-\pi^+\pi^0$, 88.8% of this channel is reconstructed in $2\pi^-\pi^+\pi^0\,\nu_\tau$ and $2\pi^-\pi^+2\pi^0\,\nu_\tau$, respectively
[3] Through $\eta \to 2\gamma$, 39.3% of this channel is reconstructed in $\pi^-3\pi^0\,\nu_\tau$

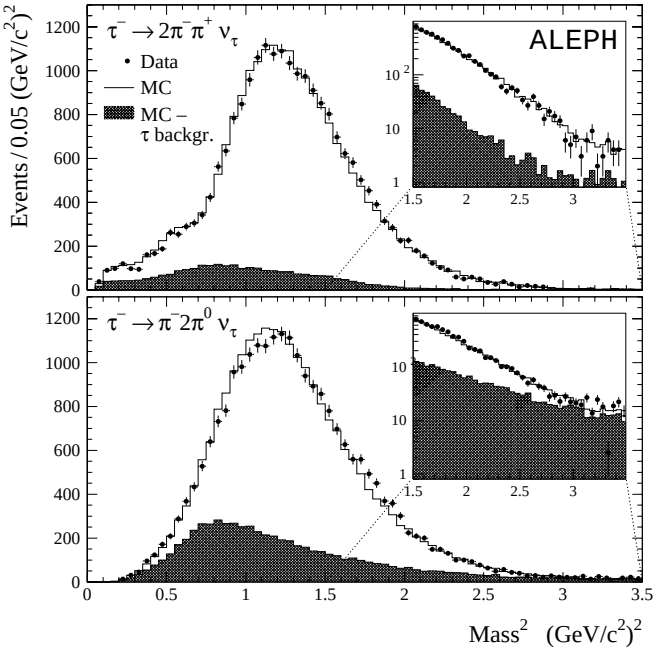

Fig. 2. Invariant mass-squared distributions of the decays $\tau^- \to 2\pi^-\pi^+\,\nu_\tau$ and $\tau^- \to \pi^-2\pi^0\,\nu_\tau$

in [1] using isospin symmetry. However, one has to account for the fact that the six-pion channel is contaminated by isospin-violating $\tau^- \to \eta\,2\pi^-\pi^+\,\nu_\tau$, $\eta\,\pi^-2\pi^0\,\nu_\tau$ decays. These were reported for the first time by the CLEO Collaboration [31].

The small fraction of the $\omega\,\pi^-\,\nu_\tau$ decay channel that is not reconstructed in the four-pion final state is added using the simulation. Similarly, one corrects for $\eta\,\pi^-\pi^0\,\nu_\tau$ decay modes other than $\eta \to 2\gamma$ which is classified in the $h^-3\pi^0\,\nu_\tau$ final state, since the two photon mass is inconsistent with the π^0 mass so that each photon is reconstructed as a π^0.

The $K^-\,K^0\,\nu_\tau$ mass distribution is taken entirely from the simulation. The $K\bar{K}\pi$ modes are conservatively assumed to be (50±50)% vector and axial-vector. The corresponding spectral functions are obtained from the Monte Carlo simulation. This is further discussed in [1]. Taking both vector and axial-vector parts as $(50 \pm 50)\%$, the vector part of the total $K\bar{K}\pi\pi$ branching ratio is estimated to be $(0.08 \pm 0.08)\%$.

The invariant mass spectra of the small contributions labeled "MC" in Figs. 1 and 5 are taken from the Monte Carlo simulation accompanied by a channel-dependent systematic error of up to 50% of the bin entry.

4.4 Axial-vector spectral functions

Exclusively measured axial-vector modes are the three-pion final states, occurring in both $2\pi^-\pi^+\,\nu_\tau$ and $\pi^-2\pi^0\,\nu_\tau$, and the five-pion modes $3\pi^-2\pi^+\,\nu_\tau$ and $2\pi^-\pi^+2\pi^0\,\nu_\tau$. The corresponding invariant mass-squared spectra before unfolding are depicted for data and Monte

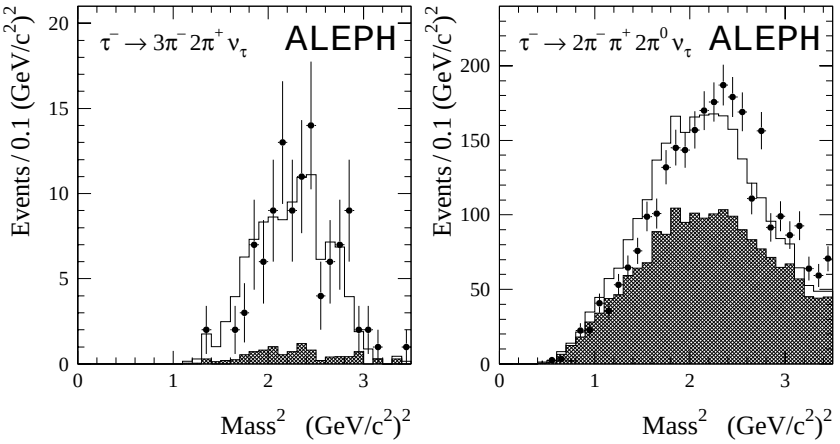

Fig. 3. Invariant mass-squared distributions of the decays $\tau^- \to 3\pi^- 2\pi^+ \nu_\tau$ and $\tau^- \to 2\pi^- \pi^+ 2\pi^0 \nu_\tau$. The points are the ALEPH data, the histograms represent the simulation and the hatched areas are the expected τ background distributions according to the simulation

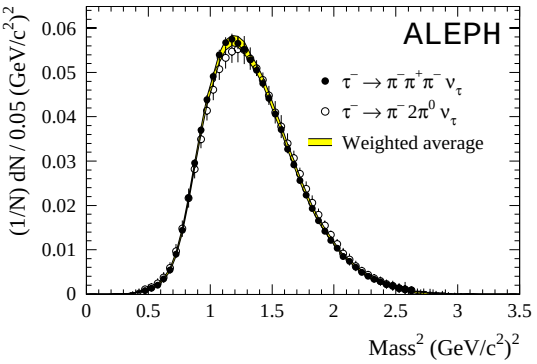

Fig. 4. Unfolded (physical) invariant mass-squared spectra of the τ final states $2\pi^-\pi^+\nu_\tau$ and $\pi^- 2\pi^0 \nu_\tau$ and their weighted average

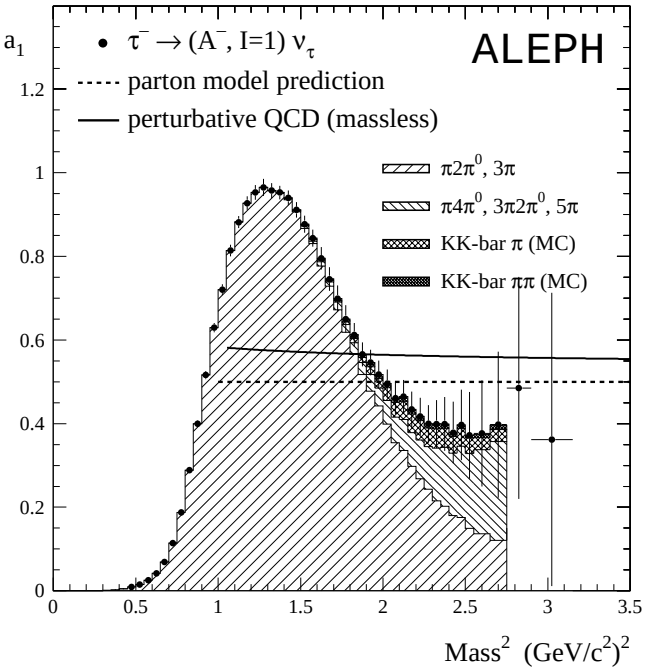

Fig. 5. Total inclusive τ axial-vector current spectral function (without the pion pole). The lines show the prediction from the naive parton model and from massless perturbative QCD using $\alpha_s(M_Z^2) = 0.120$

Carlo simulation in Figs. 2 and 3. The small shoulder seen in the measured $2\pi^-\pi^+\nu_\tau$ spectrum around 0.3 GeV^2 mass-squared (upper plot in Fig. 2) stems from decays where only two tracks are reconstructed and the invariant mass as a result is underestimated. Due to incomplete ECAL energy collection, the measured $\pi^- 2\pi^0 \nu_\tau$ distribution is slightly shifted to lower masses. These features are well reproduced by the detector simulation.

For both three-pion decay modes, the τ decay library `TAUOLA1.5` is used as physics input for the detector simulation. It employs the Kühn-Santamaria parametrization [38] based on a dominant large $a_1^-(1260)$ resonance, $\Gamma_{a_1(1260)} = 0.4$ GeV/c^2, which decays into $\rho^-(770)\pi^0 \to \pi^- 2\pi^0$ or $\rho^0(770)\pi^- \to 2\pi^-\pi^+$ with interference between the two $\rho\pi$ combinations. Scalar contributions to the three pion decay, e.g., $\pi(1300) \to \rho\pi$, suppressed by the PCAC theorem and by angular momentum considerations, are neglected in this model. However, the measurement of the spectral functions and in particular the unfolding procedure is essentially independent of the physics input into the simulation.

Figure 4 shows the unfolded $2\pi^-\pi^+\nu_\tau$ and $\pi^- 2\pi^0 \nu_\tau$ mass spectra with reasonable agreement in form and normalization ($\chi^2 = 41.4$ per 59 degrees of freedom). In the following both channels are assumed to have identical spectra so that it is appropriate to use the weighted average of the distributions for the inclusive axial-vector spectral function[1].

[1] The weighted average is calculated between two intrinsically correlated distributions. The averaged distribution k with bin entries k_i, $i = 1, \ldots, N_{\rm bin}$ is defined to minimize $\chi^2 = (x_{(--+)} - k)C^{-1}_{(--+)}(x_{(--+)} - k) + (x_{(-00)} - k)C^{-1}_{(-00)}(x_{(-00)} - k)$, where the indices denote the charges of the τ final states, x are the mass-squared distributions and C^{-1} the corresponding inverted covariance matrices. The weighted average is then the solution of the system of linear equations $x_{(--+)}C^{-1}_{(--+)} + x_{(-00)}C^{-1}_{(-00)} = k(C^{-1}_{(--+)} + C^{-1}_{(-00)})$, and the covariance matrix of the average satisfies $C_k^{-1} = C^{-1}_{(--+)} + C^{-1}_{(-00)}$

4.4.1 The inclusive τ axial-vector spectral function

In complete analogy to the vector spectral function the inclusive axial-vector spectral function is obtained by summing up the exclusive axial-vector spectral functions with the addition of small unmeasured modes taken from the Monte Carlo simulation. The right column of Table 1 gives a compilation of the exclusive axial-vector branching ratios used:

- The five-pion spectral functions are only measured in the $2\pi^-\pi^+2\pi^0\,\nu_\tau$ and $3\pi^-2\pi^+\,\nu_\tau$ final states. Using Pais' isospin classes [39], the branching fraction of $\pi^-4\pi^0\,\nu_\tau$ can be bounded entirely using the $3\pi^-2\pi^+\,\nu_\tau$ branching fraction: $B_{\pi^\pm 4\pi^0} \leq 3/4 \times B_{5\pi^\pm} = 0.054\%$. Half of this upper limit is taken with an error of 100%.
- As in the vector case, the small fraction of the $\omega\,\pi^-\pi^0\,\nu_\tau$ decay channel that is not accounted for in the $2\pi^-\pi^+2\pi^0\,\nu_\tau$ final state is added from the simulation.
- Also considered are the axial-vector $\eta\,(3\pi)^-\,\nu_\tau$ final states [31]. CLEO observed that the dominant part of it issues from the $\tau^-\to \mathrm{f_1}(1285)\pi^-$ intermediate state, with $B(\tau^-\to \mathrm{f_1}\pi^-\,\nu_\tau) = (0.068 \pm 0.030)\%$, measured in the $\mathrm{f_1} \to \eta\,\pi^+\pi^-$ and $\mathrm{f_1} \to \eta\,\pi^0\pi^0$ decay modes [31]. Since the $\mathrm{f_1}$ meson is isoscalar, the branching ratios relate as $B(\tau^- \to \eta\,2\pi^-\pi^+\,\nu_\tau) = 2 \times B(\tau^- \to \eta\,\pi^-2\pi^0\,\nu_\tau)$. The distributions are taken from the ordinary six-pion phase space simulation accompanied by large systematic errors.
- The $\mathrm{K\bar{K}}\pi$ and $\mathrm{K\bar{K}}\pi\pi$ final states contribute with $(50\pm 50)\%$ to the inclusive axial-vector spectral function, with full anticorrelation to the inclusive vector spectral function. Both invariant mass distributions are taken from the simulation.

The total inclusive axial-vector spectral function is plotted in Fig. 5 together with the naive parton model and the massless, perturbative QCD prediction. One observes that the asymptotic region is apparently not reached at the τ mass scale.

4.5 The $(v_1 \pm a_1)$ spectral functions

For the total (v_1+a_1) hadronic spectral function one does not have to distinguish the current properties of the non-strange hadronic τ decay channels. Hence the mixture of all contributing non-strange final states is measured inclusively using the following procedure.

The two- and three-pion final states dominate and their exclusive measurements are added with proper accounting for the correlations. The remaining contributing topologies are treated inclusively, i.e., without separation of the vector and axial-vector decay modes. This reduces the statistical uncertainty. The effect of the feedthrough between τ final states on the invariant mass spectrum is described by the Monte Carlo simulation and thus corrected in the data unfolding. In this procedure the simulated mass distributions are iteratively corrected using the exclusive vector/axial-vector unfolded mass spectra. Another advantage of the inclusive (v_1+a_1) measurement is that one does not have to separate the vector/axial-vector currents of the $\mathrm{K\bar{K}}\pi$ and $\mathrm{K\bar{K}}\pi\pi$ modes. The (v_1+a_1) spectral function is depicted in Fig. 6. The improvement in precision in comparison to an exclusive sum of Fig. 1 and Fig. 5 is obvious at higher mass-squared. One clearly sees the oscillating behaviour of the spectral function but, unlike the vector/axial-vector spectral functions, this does approximately reach the asymptotic limit predicted by perturbative QCD at $s \to M_\tau^2$.

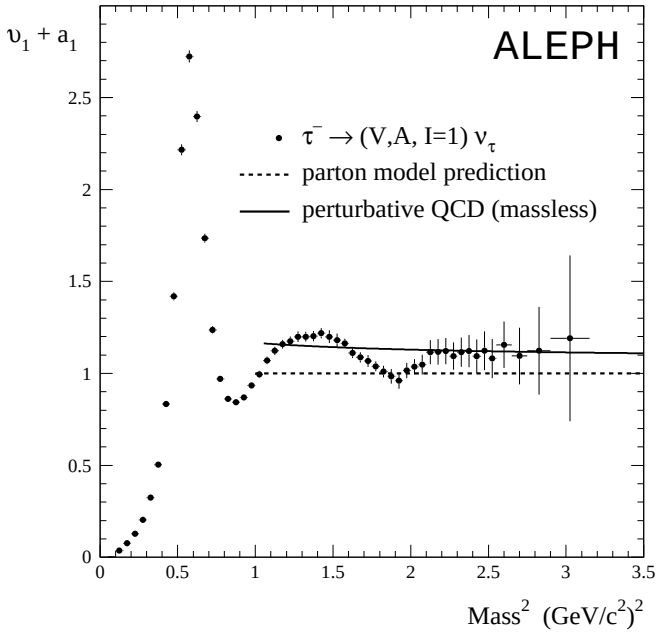

Fig. 6. Inclusively measured vector plus axial-vector (v_1+a_1) spectral function and predictions from the parton model and from massless perturbative QCD using $\alpha_s(M_Z^2) = 0.120$

In the case of the (v_1-a_1) spectral function, uncertainties on the V/A separation are reinforced due to their complete anticorrelation. In addition, anticorrelations given in [26] between τ final states with adjacent numbers of pions increase the errors. The $(v_1 - a_1)$ spectral function is shown in Fig. 7. The oscillating behaviour of the respective v_1 and a_1 spectral functions is emphasized and the asymptotic behaviour is clearly not attained at M_τ^2.

5 Chiral sum rules

The application of chiral symmetry leads to low energy sum rules involving the difference of vector and axial-vector spectral functions by virtue of the optical theorem. These sum rules are dispersion relations between real and absorptive parts of a two-point correlation function that transforms symmetrically under $SU(2)_L \times SU(2)_R$ in the case of non-strange currents. Corresponding integrals are:

$$\frac{1}{4\pi^2}\int_0^{s_0\to\infty} ds\,\frac{1}{s}\,[v_1(s) - a_1(s)] = f_\pi^2\,\frac{\langle r_\pi^2\rangle}{3} - F_A\ , \quad (5)$$

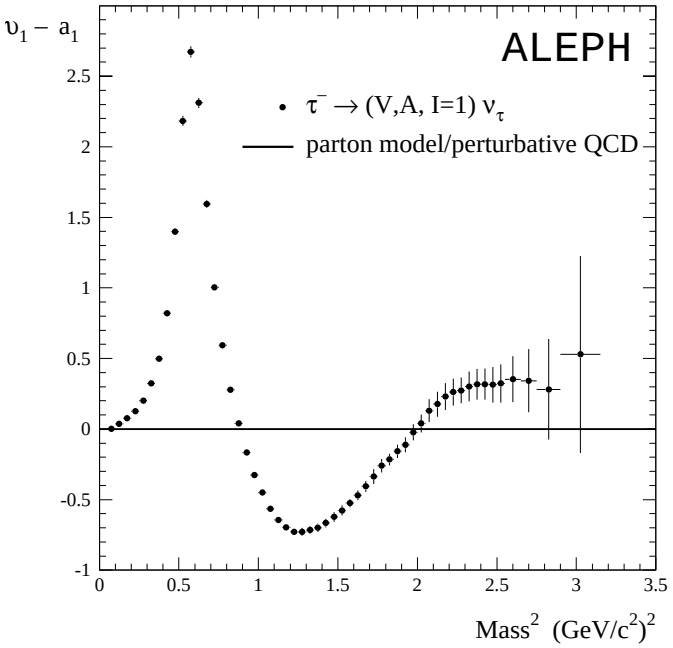

Fig. 7. Inclusively measured vector minus axial-vector ($v_1 - a_1$) spectral function. In the parton model as well as in perturbative QCD vector and axial-vector contributions are degenerate

$$\frac{1}{4\pi^2}\int_0^{s_0\to\infty} ds\ [v_1(s)-a_1(s)] = f_\pi^2\ , \tag{6}$$

$$\frac{1}{4\pi^2}\int_0^{s_0\to\infty} ds\, s\ [v_1(s)-a_1(s)] = 0\ , \tag{7}$$

$$\frac{1}{4\pi^2}\int_0^{s_0\to\infty} ds\, s \ln\frac{s}{\lambda^2}\ [v_1(s)-a_1(s)] = -\frac{4\pi f_\pi^2}{3\alpha} \times(m_{\pi^\pm}^2 - m_{\pi^0}^2)\ . \tag{8}$$

Equation (5) is known as the Das-Mathur-Okubo (DMO) sum rule [32]. It relates the given integral to the square of the pion decay constant $f_\pi = (92.4 \pm 0.3)$ MeV [11] obtained from the decays $\pi^- \to \mu^-\bar\nu_\mu$ and $\pi^- \to \mu^-\bar\nu_\mu\gamma$, to the pion axial-vector form factor F_A for radiative decays $\pi^- \to \ell^-\bar\nu_\ell\gamma$, and to the pion charge radius-squared $\langle r_\pi^2\rangle = (0.439 \pm 0.008)$ fm^2 obtained from a one parameter fit to space-like data [33]. Equations (6) and (7) are the first and the second Weinberg sum rules (WSR) [34]. When switching quark masses on, only the first WSR remains valid while the second WSR breaks down due to contributions from the difference of non-conserved vector and axial-vector currents of order m_q^2/s, leading to a quadratic divergence of the integral. Equation (8) represents the electromagnetic splitting of the pion masses [35]. Although apparently containing an arbitrary renormalization scale λ, the sum rule is actually independent of λ by virtue of the second WSR (7). Only for s_0 values for which (7) has not reached convergence does (8) maintains its λ dependence.

The above integrals are calculated with variable upper integration bounds $s_0 \le M_\tau^2$ using the spectral functions and their respective covariance matrices in order to provide a straightforward gaussian error propagation taking into account the strong bin-to-bin correlations of the spectral functions. Also considered are the anticorrelations between v_1 and $a_{1,0}$ due to the estimates of the vector/axial-vector parts of the final states K$\bar{\rm K}\pi$ and K$\bar{\rm K}\pi\pi$ and the τ hadronic branching ratios.

The sum rules (5)–(8) versus the upper integration bound $s_0 \le M_\tau^2$ are plotted in Figs. 8a–d. The horizontal band depicts the corresponding chiral predictions of the integrals taken from [36]. One observes that only for the DMO sum rule (Fig. 8a), for which contributions from higher mass-squares are suppressed, does the saturation within the one sigma error seem to occur at the τ mass scale. The other sum rules (Fig. 8b,c) are apparently not saturated at M_τ^2 (non-zero slope) as indicated by the non-vanishing $(v_1 - a_1)$ spectral function at the end of the τ phase space (Fig. 7) and its oscillatory behaviour. More quantitative studies of the sum rules can be found in [24].

6 The measurement of $\alpha_s(M_\tau^2)$

The measurement of $\alpha_s(M_\tau^2)$ presented in this section adopts a method based on a simultaneous fit of QCD parametrizations with perturbative and nonperturbative components to the ratio R_τ defined as

$$R_\tau = \frac{\Gamma(\tau^- \to \text{hadrons}^-\,\nu_\tau)}{\Gamma(\tau^- \to e^-\,\bar\nu_e\nu_\tau)}\ , \tag{9}$$

and to the spectral moments defined below (Sect. 6.4). It was proposed by F. Le Diberder and A. Pich [6] and has been employed in previous analyses by the ALEPH [2] and CLEO [3] Collaborations.

6.1 Theoretical prediction for R_τ

According to (4) the imaginary parts of the vector and axial-vector two-point correlation functions $\Pi^{(J)}_{\bar ud,V/A}(s)$, with the spin J of the hadronic system, are proportional to the τ hadronic spectral functions with corresponding quantum numbers. The non-strange ratio R_τ can be written as an integral of these spectral functions over the invariant mass-squared s of the final state hadrons [5]:

$$R_\tau(s_0) = 12\pi S_{\rm EW}\int_0^{s_0}\frac{ds}{s_0}\left(1-\frac{s}{s_0}\right)^2\left[\left(1+2\frac{s}{s_0}\right) \times{\rm Im}\Pi^{(1)}(s+i\epsilon) + {\rm Im}\Pi^{(0)}(s+i\epsilon)\right]\ , \tag{10}$$

where $\Pi^{(J)}$ can be decomposed as $\Pi^{(J)} = |V_{ud}|^2 \times \left(\Pi^{(J)}_{ud,V} + \Pi^{(J)}_{ud,A}\right)$. The correlation function $\Pi^{(J)}$ is analytic in the complex s plane everywhere except on the positive real axis where singularities exist. Hence by Cauchy's

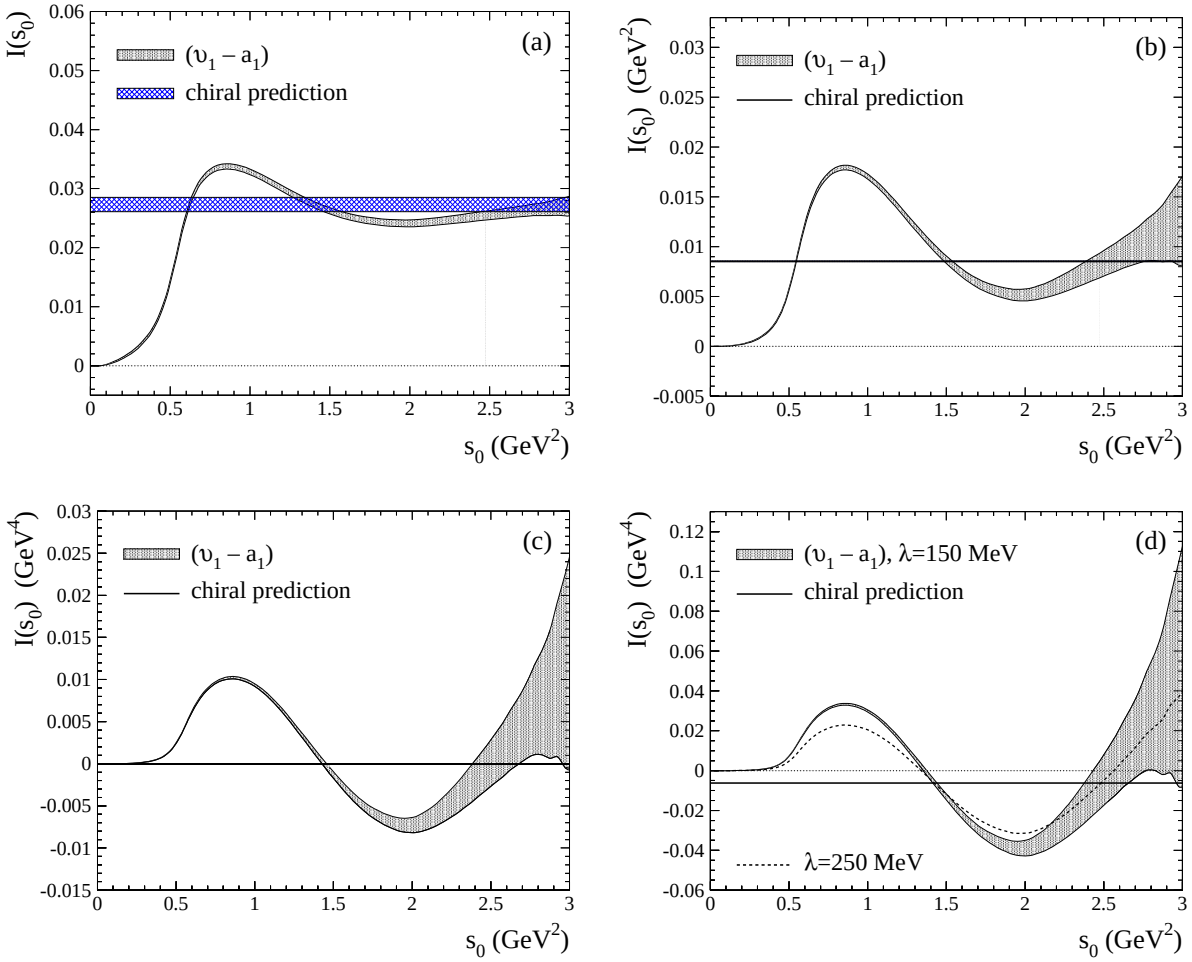

Fig. 8. Sum rules corresponding to (5)–(8) (plots: a–d) versus the upper integration bound s_0

theorem, the imaginary part of $\Pi^{(J)}$ is proportional to the discontinuity across the positive real axis.

The energy scale s_0 for $s_0 = M_\tau^2$ is large enough that contributions from nonperturbative effects be small. It is therefore assumed that one can use the *Operator Product Expansion* (OPE) to organize perturbative and nonperturbative contributions to $R_\tau(s_0)$. The factor $(1 - s/s_0)^2$ suppresses the contribution from the region near the positive real axis where $\Pi^{(J)}(s)$ has a branch cut and OPE validity is restricted [40].

The theoretical prediction of the vector and axial-vector ratio $R_{\tau,V/A}$ can thus be written as:

$$R_{\tau,V/A} = \frac{3}{2}|V_{ud}|^2 S_{\rm EW}\left(1 + \delta^{(0)} + \delta'_{\rm EW} + \delta^{(2-{\rm mass})}_{ud,V/A} + \sum_{D=4,6,\ldots} \delta^{(D)}_{ud,V/A}\right) , \qquad (11)$$

with the residual non-logarithmic electroweak correction $\delta'_{\rm EW} = 0.0010$ [41], neglected in the following, and the dimension $D = 2$ contribution $\delta^{(2-{\rm mass})}_{ud,V/A}$ from quark masses which is lower than 0.1% for u, d quarks. The term $\delta^{(0)}$ is the purely perturbative contribution, while the $\delta^{(D)}$ are the OPE terms in powers of $s_0^{-D/2}$:

$$\delta^{(D)}_{ud,V/A} = \sum_{\dim\mathcal{O}=D} C_{ud,V/A}(s,\mu)\frac{\langle\mathcal{O}_{ud}(\mu)\rangle_{V/A}}{(-s_0)^{D/2}} , \qquad (12)$$

where the parameter μ separates the long-distance nonperturbative effects, absorbed into the vacuum expectation elements $\langle\mathcal{O}_{ud}(\mu)\rangle$, from the short-distance effects which are included in the Wilson coefficients $C_{ud,V/A}(s,\mu)$ [42].

6.2 Perturbative prediction

The perturbative prediction adopted in this analysis follows in detail [7]. The perturbative contribution is given in the chiral limit. Effects from quark masses have been calculated in [43] and are found to be well below 1% for the light quarks. Thus the contributions from vector and axial-vector currents coincide to any given order of perturbation theory and the results are flavour independent.

The perturbative contribution in (11) is then given by [7]

$$1 + \delta^{(0)} = \sum_{n=0}^{3} K_n A^{(n)}(\alpha_s) , \qquad (13)$$

with $K_0 = K_1 = 1$, $K_2 = 1.63982$ and $K_3 = 6.37101$ for three active flavours in the $\overline{\rm MS}$ scheme [37]. The coefficients K_n are known up to three-loop order α_s^3 and for $n \geq 2$ they depend on the renormalization scheme employed. The functions $A^{(n)}(\alpha_s)$ in (13) are the contour integrals

$$A^{(n)}(\alpha_s) = \frac{1}{2\pi i} \oint\limits_{|s|=s_0} \frac{ds}{s} \left[1 - 2\frac{s}{s_0} + 2\left(\frac{s}{s_0}\right)^3 - \left(\frac{s}{s_0}\right)^4\right] \times \left(\frac{\alpha_s(-s)}{\pi}\right)^n , \quad (14)$$

where the contour runs counter clockwise around the circle from $s_0 + i\epsilon$ to $s_0 - i\epsilon$. The strong coupling constant in the vicinity of s_0 can be expanded in powers of $\alpha_s(s_0)$, with coefficients that are polynomials in $\ln(s/s_0)$ [5]. The perturbative prediction becomes then a function of the K_n coefficients and elementary integrals. Up to fourth order the fixed-order perturbation theory (FOPT) expansion reads

$$1 + \delta_{\rm E}^{(0)} = 1 + \frac{\alpha_s(s_0)}{\pi} + 5.2023\left(\frac{\alpha_s(s_0)}{\pi}\right)^2 + 26.366\left(\frac{\alpha_s(s_0)}{\pi}\right)^3 + (K_4 + 78.00)\left(\frac{\alpha_s(s_0)}{\pi}\right)^4, \quad (15)$$

with the unknown K_4 coefficient.

Another approach to the solution of the contour integral (14) is to perform a direct numerical evaluation using the solution of the renormalization group equation (RGE) to four-loops [44] as input for the running $\alpha_s(-s)$ [45, 7]. It provides a resummation of all known higher order logarithmic integrals and improves the convergence of the perturbative series. While, for instance, the third order term in the expansion (15) contributes with 17% to the total (truncated) perturbative prediction, the corresponding term of the numerical solution amounts only to 6.6% (assuming $\alpha_s(M_\tau^2) = 0.35$). This numerical solution of (13) will be referred as *contour-improved* fixed-order perturbation theory ($\rm FOPT_{CI}$) in the following.

Despite a number of arguments expressed in [7], the intrinsic ambiguity between FOPT and $\rm FOPT_{CI}$ is unresolvable at present. This is due to the truncation of the perturbative approximation of $\delta^{(0)}$ at finite order in α_s. A conservative measure of this ambiguity is obtained from the deviation in R_τ found when cutting all additional orders in α_s (which is FOPT) and keeping them ($\rm FOPT_{CI}$), respectively. Both methods are likewise considered in this analysis.

6.3 Nonperturbative contributions

Following SVZ [4], the first contribution to $R_\tau(s_0)$ beyond the $D = 0$ perturbative expansion is the non-dynamical quark mass correction of dimension $D = 2$, i.e., corrections in powers of $1/s_0$. They have been calculated up to next-to-leading order α_s [46].

The dimension $D = 4$ operators have dynamical contributions from the gluon condensate $\langle(\alpha_s/\pi)GG\rangle$ and quark condensates $m_u\langle 0|\bar{u}u|0\rangle$, $m_d\langle 0|\bar{d}d|0\rangle$ of the light u, d quarks. Remaining $D = 4$ operators are the running quark masses to the fourth power. The contribution of the gluon condensate to $R_{\tau,V/A}$ vanishes in first order $\alpha_s(s_0)$. However, there appear second order terms in the Wilson coefficients due to the logarithmic s dependence of $\alpha_s(s)$ which after performing the integral (10) becomes $\alpha_s^2(s_0)$.

The contributions from dimension $D = 6$ operators are rather complex. The large number of independent operators of the four-quark type occurring can be reduced by means of the vacuum saturation approximation [4,5] to leading order α_s. The operators are then expressed as products of scale dependent two-quark condensates of the type $\alpha_s(\mu)\langle\bar{q}_i q_i(\mu)\rangle\langle\bar{q}_j q_j(\mu)\rangle$. Since the vacuum saturation approximation is a simplifying assumption, possible deviations are accounted for by introducing an effective scale independent operator of the form $\rho\alpha_s\langle\bar{q}q\rangle^2$ that is fit to the data.

The dimension $D = 8$ contribution has a structure of non-trivial quark-quark, quark-gluon and four-gluon condensates the explicit form of which is given for the vector case in [47]. For the theoretical prediction of $R_\tau(s_0)$ used here, the complete long and short distance part is absorbed into the scale invariant phenomenological $D = 8$ operator $\langle\mathcal{O}_8\rangle$.

Higher order contributions from $D \geq 10$ operators are expected to be small as, equivalent to the gluon condensate, constant terms and terms in leading order α_s vanish in (10) after integration.

The formulae are taken entirely from [5], in which (10) is evaluated after the power terms (12) are inserted into the integral.

6.4 Spectral moments

It was shown in [6] that it is possible to benefit from the information provided by the explicit shape of the spectral functions in order to obtain additional constraints on $\alpha_s(s_0)$ and – more importantly – on the nonperturbative condensates. The spectral moments at M_τ^2 are defined as:

$$R_{\tau,V/A}^{kl} \equiv \int\limits_0^{M_\tau^2} ds \left(1 - \frac{s}{M_\tau^2}\right)^k \left(\frac{s}{M_\tau^2}\right)^l \frac{dR_{\tau,V/A}}{ds} , \quad (16)$$

with $R_{\tau,V/A}^{00} = R_{\tau,V/A}$. The factor $(1 - s/M_\tau^2)^k$ suppresses the integrand at the crossing of the positive real axis where the validity of the OPE is less certain and the experimental accuracy is statistically limited. Its counterpart $(s/M_\tau^2)^l$ projects out higher energies. The new spectral information is used to fit simultaneously $\alpha_s(M_\tau^2)$ and the phenomenological operators $\langle(\alpha_s/\pi)GG_{D=4}\rangle$, $\langle\mathcal{O}_{D=6}\rangle$ and $\langle\mathcal{O}_{D=8}\rangle$. Due to the intrinsic strong correlations only five moments are used as input to the fits.

In analogy to R_τ the contributions to the moments originating from perturbative and nonperturbative QCD

are separated via the OPE. The prediction of the perturbative contribution takes then the form

$$\delta^{(0,kl)} \;=\; \sum_{n=1}^{3} K_n A^{(n,kl)}(\alpha_s) \;, \tag{17}$$

with contour integrals $A^{(n,kl)}(\alpha_s)$ [6] that are expanded up to $\alpha_s^3(s)$ (FOPT) or numerically resolved for the running $\alpha_s(-s)$ obtained from the RGE ($\mathrm{FOPT_{CI}}$).

In the chiral limit and neglecting the logarithmic s dependence of the Wilson coefficients, the dimension $D = 2, 4, 6, 8$ nonperturbative contributions to the moments read

$$\delta^{(D,kl)}_{ud,V/A} = 8\pi^2 \begin{pmatrix} (D=2) & (D=4) & (D=6) & (D=8) & (k,l) \\ 1 & 0 & -3 & -2 & (0,0) \\ 1 & 1 & -3 & -5 & (1,0) \\ 0 & -1 & -1 & 3 & (1,1) \\ 0 & 0 & 1 & 1 & (1,2) \\ 0 & 0 & 0 & -1 & (1,3) \end{pmatrix} \times \sum_{\dim\mathcal{O}=D} C(\mu) \frac{\langle \mathcal{O}(\mu) \rangle}{M_\tau^D} \;, \tag{18}$$

where the matrix is defined by the choice of the coefficients for the moments $k = 1$, $l = 0, 1, 2, 3$. It can be seen that with increasing weight l the low dimension operators give no contributions.

For practical purpose it is more convenient to define moments that are normalized to the corresponding $R_{\tau,V/A}$ in order to decouple the normalization from the shape of the τ spectral functions:

$$\begin{aligned} D^{kl}_{\tau,V/A} &\equiv \frac{R^{kl}_{\tau,V/A}}{R_{\tau,V/A}} \\ &= \int_0^{M_\tau^2} ds \left(1 - \frac{s}{M_\tau^2}\right)^k \left(\frac{s}{M_\tau^2}\right)^l \frac{1}{N_{V/A}} \frac{dN_{V/A}}{ds} \;. \end{aligned} \tag{19}$$

There now exist two sets of experimentally almost uncorrelated observables — $R_{\tau,V/A}$ and spectral moments — which provide independent constraints on $\alpha_s(M_\tau^2)$ and thus an important test of consistency.

6.5 Measurement of R_τ and the moments

The ratio of non-strange hadronic width and electronic branching ratio is calculated from the difference of the ratio of the total hadronic width and electronic branching ratio,

$$\begin{aligned} R_\tau &= \frac{1 - B(\tau^- \to e^- \bar{\nu}_e \nu_\tau) - B(\tau^- \to \mu^- \bar{\nu}_\mu \nu_\tau)}{B(\tau^- \to e^- \bar{\nu}_e \nu_\tau)} \\ &= \frac{1}{B(\tau^- \to e^- \bar{\nu}_e \nu_\tau)} - 1.9726 \\ &= 3.647 \pm 0.014 \;, \end{aligned} \tag{20}$$

obtained from the world average value (3), and the strange width ratio,

$$R_{\tau,S} = 0.155 \pm 0.008 \;, \tag{21}$$

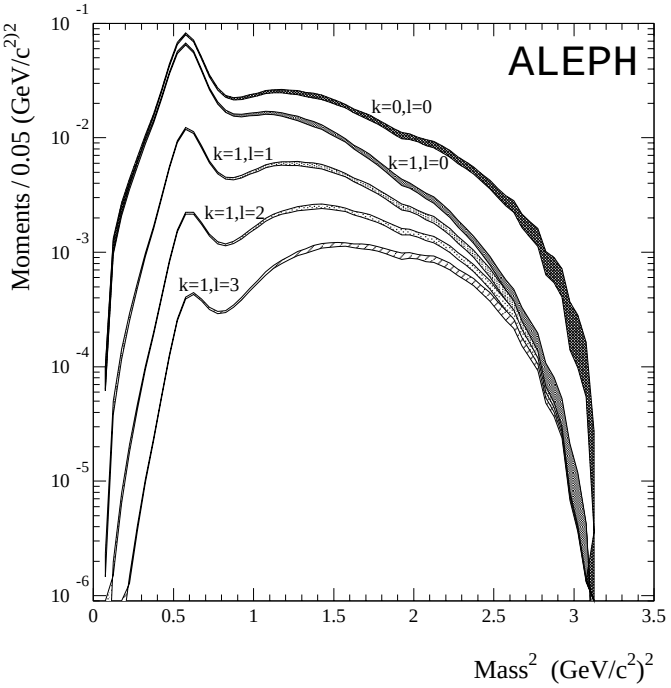

Fig. 9. $(V + A)$ weighted invariant mass-squared spectra for $k = 1$, $l = 0, \ldots, 3$ (without the pion pole) according to the integrand in (19)

taken from [48], yielding the result

$$R_{\tau,V+A} = 3.492 \pm 0.016 \;. \tag{22}$$

There is no advantage in including $R_{\tau,S}$ (or equivalently using R_τ) in this analysis, because the strange quark sector introduces another parameter, the strange quark mass, which the additional data is used to fit [49]. Computing the ratio of the inclusive vector and axial-vector branching fractions taken from Table 1, to the electronic branching fraction yields

$$R_{\tau,V} = 1.775 \pm 0.017 \;, \tag{23}$$

$$R_{\tau,A} = 1.717 \pm 0.018 \;. \tag{24}$$

The normalization according to (19) reduces considerably the correlation between R_τ and the moments. It is completely negligible in the $(V + A)$ case where $R_{\tau,V+A}$ is calculated from the difference $R_\tau - R_{\tau,S}$, which has no correlations with the hadronic invariant mass spectrum. Figure 9 shows the integrand in (19) for $k = 1, l = 0, \ldots, 3$ as a function of s.

As can be concluded from (18), higher moments in l determine higher dimensional OPE terms. The effect of a variation of α_s and, e.g., $\delta^{(8)}$ on $R_{\tau,V+A}$ and the moments is shown in Fig. 10. It demonstrates the constraints of the measured observables on the QCD quantities. The central points and error bars are the theoretical predictions for $R_{\tau,V+A}$ and the moments for some input values $\alpha_s(M_\tau^2)$, $\delta^{(4)}$, $\delta^{(6)}$ and $\delta^{(8)}$, and the propagated errors of one standard deviation (Δ). The stars depict the shift when changing $\alpha_s \to \alpha_s + 2\Delta\alpha_s$, while the triangles show

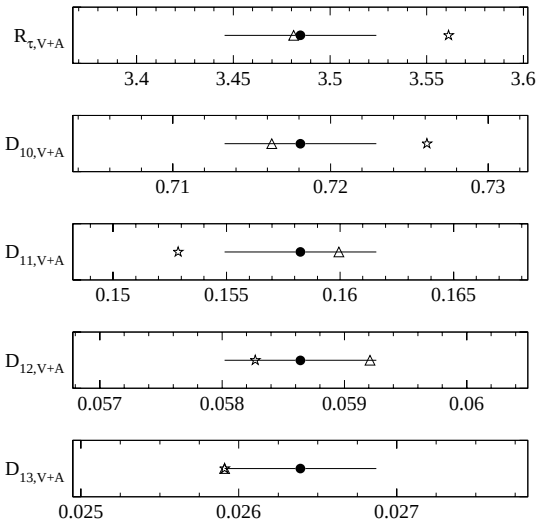

Fig. 10. Effect of a $\alpha_s \to \alpha_s + 2\Delta\alpha_s$ (hollow stars) and $\delta^{(8)} \to \delta^{(8)} + 2\Delta\delta^{(8)}$ (hollow triangles) shift on $R_{\tau,V+A}$ and the $(V+A)$ moments (using $\mathrm{FOPT_{CI}}$). The points in the centres give the unshifted reference values

Table 2. Spectral Moments of vector (V), axial-vector (A) and vector plus axial-vector ($V+A$) inclusive τ decays. The errors give the total experimental uncertainties including statistical and systematic effects

ALEPH	$l=0$	$l=1$	$l=2$	$l=3$
D_V^{1l}	0.7173	0.1687	0.0529	0.0225
$\Delta^{\exp} D_V^{1l}$	0.0035	0.0006	0.0007	0.0006
D_A^{1l}	0.7180	0.1472	0.0642	0.0306
$\Delta^{\exp} D_A^{1l}$	0.0040	0.0012	0.0007	0.0005
D_{V+A}^{1l}	0.7177	0.1581	0.0585	0.0265
$\Delta^{\exp} D_{V+A}^{1l}$	0.0022	0.0006	0.0004	0.0004

what happens when shifting $\delta^{(8)} \to \delta^{(8)} + 2\Delta\delta^{(8)}$. One observes that $\alpha_s(M_\tau^2)$ is primarily determined from $R_{\tau,V+A}$ and the first moments D_{V+A}^{10}, D_{V+A}^{11}. On the other hand, D_{V+A}^{12} and D_{V+A}^{13} constrain the high dimensional nonperturbative power terms, while their effect on $\alpha_s(M_\tau^2)$ is weak.

The measured values of the moments for V, A and the $(V+A)$ spectral functions are given in Table 2 and their correlation matrices in Table 3. The correlations between the moments are computed analytically from the contraction of the derivatives of two involved moments with the covariance matrices of the respective normalized invariant mass-squared spectra. In all cases, the negative sign between the $k=1, l=0$ and the $k=1, l\geq 1$ moments is understood to be due to the ρ and the π, a_1 peaks which determine the major part of the $k=1, l=0$ moments. They are much less important for higher moments as one can see in Fig. 9 and consequently the amount of negative correlation increases with $l=1,2,3$. This also explains the large and increasing positive correlations between the

Table 3. Experimental correlations between the moments $D_{\tau,V/A/V+A}^{kl}$. There are no correlations between $R_{\tau,V+A}$ and the corresponding moments

ALEPH	$D_{\tau,V}^{10}$	$D_{\tau,V}^{11}$	$D_{\tau,V}^{12}$	$D_{\tau,V}^{13}$
$R_{\tau,V}$	−0.56	0.33	0.58	0.56
$D_{\tau,V}^{10}$	1	−0.21	−0.87	−0.95
$D_{\tau,V}^{11}$	–	1	0.63	0.39
$D_{\tau,V}^{12}$	–	–	1	0.96
$D_{\tau,V}^{13}$	–	–	–	1

ALEPH	$D_{\tau,A}^{10}$	$D_{\tau,A}^{11}$	$D_{\tau,A}^{12}$	$D_{\tau,A}^{13}$
$R_{\tau,A}$	−0.52	0.24	0.48	0.56
$D_{\tau,A}^{10}$	1	−0.41	−0.81	−0.96
$D_{\tau,A}^{11}$	–	1	0.83	0.51
$D_{\tau,A}^{12}$	–	–	1	0.90
$D_{\tau,A}^{13}$	–	–	–	1

ALEPH	$D_{\tau,V+A}^{10}$	$D_{\tau,V+A}^{11}$	$D_{\tau,V+A}^{12}$	$D_{\tau,V+A}^{13}$
$D_{\tau,V+A}^{10}$	1	−0.30	−0.86	−0.96
$D_{\tau,V+A}^{11}$	–	1	0.65	0.28
$D_{\tau,V+A}^{12}$	–	–	1	0.91
$D_{\tau,V+A}^{13}$	–	–	–	1

$k=1, l\geq 1$ moments, in which, with growing l, the high energy tail becomes more important than the low energy peaks. The individual contributions to the total errors are listed in Table 4 for the $(V+A)$ case. One clearly sees the dominance from the hadronic branching ratio uncertainties which is also the only relevant error contributing to $R_{\tau,V/A}$.

The new measurement of the $(V+A)$ spectral moments can be compared to publications which are already available from ALEPH and CLEO (Fig. 11). The previous ALEPH measurements contain the Cabibbo suppressed final states so that the comparisons to CLEO and to this analysis must be done with care. One observes a shift of the first moment $k=1, l=0$ to lower values and, corresponding to their anti-correlations, larger values for the $k=1, l\geq 1$ moments in the new analysis when compared to the former ones. This is partially explained by the different τ branching ratios used (see open circles in Fig. 11) and the consideration of $\mathrm{K\bar{K}}$, $\mathrm{K\bar{K}}\pi$ and $\mathrm{K\bar{K}}\pi\pi$ contributions in this measurement.

6.6 The fits to the data and the theoretical uncertainties

The combined fits to the measured V, A and $(V+A)$ ratios R_τ and moments adjust the parameters $\alpha_s(M_\tau^2)$, $\langle(\alpha_s/\pi)GG\rangle$, $\langle\mathcal{O}_6\rangle_{V/A}$ and $\langle\mathcal{O}_8\rangle_{V/A}$ of the OPE in the theoretical predictions (11) and (16) of the above quantities.

These predictions are subject to uncertainties which do not differ qualitatively for either $R_{\tau,V/A}$ or the moments.

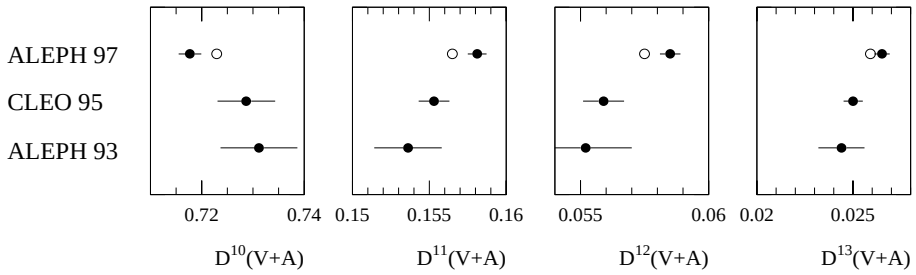

Fig. 11. Measured spectral moments D^{kl}_{V+A} in comparison to results obtained in previous analyses by CLEO in 1995 [3] and ALEPH in 1993 [2]. The ALEPH 93 results contain the strange modes. The open circles depict the present results applying the branching fractions that have been used by CLEO 95. As shown in Table 3, the moments are strongly correlated

Table 4. Relative experimental errors (in %) in the $(V + A)$ moments

Error source	$D^{10}_{\tau,V+A}$	$D^{11}_{\tau,V+A}$	$D^{12}_{\tau,V+A}$	$D^{13}_{\tau,V+A}$
Statistical error	0.10	0.12	0.18	0.35
Fake photons	0.08	0.09	0.10	0.21
ECAL energy calibration	0.03	0.06	0.08	0.20
ECAL energy resolution	0.07	0.08	0.17	0.35
Photon and π^0 reconstruction	0.10	0.09	0.12	0.31
TPC momentum calibration	0.04	0.03	0.04	0.06
TPC momentum resolution	0.02	0.01	0.02	0.05
Unfolding	0.06	0.08	0.22	0.36
MC statistics	0.05	0.06	0.11	0.33
Branching ratios	0.24	0.32	0.58	0.95
Non-τ background	0.02	0.01	0.08	0.23
MC distributions	0.05	0.04	0.17	0.30
Total	0.31	0.39	0.72	1.31

However, quantitatively, one expects larger effects, e.g., from uncertainties in the perturbative series, on $R_{\tau,V/A}$ or lower moments ($l \simeq 0, 1$). The translation from theoretical errors on the perturbative predictions of $R_{\tau,V/A}$ to $\alpha_s(M_\tau^2)$ can be derived from (11,13,15). One obtains (setting $K_4 = 50$ and $\alpha_s(M_\tau^2) = 0.35$)

$$\frac{\Delta\alpha_s(M_\tau^2)}{\Delta R_{\tau,V/A}} \approx \begin{cases} 0.88 \ (\mathrm{FOPT_{CI}}) \\ 0.56 \ \ (\mathrm{FOPT}) \end{cases}$$

and $\Delta\alpha_s(M_\tau^2)/\Delta R_{\tau,V+A} \approx 0.44$ (0.28) for $\mathrm{FOPT_{CI}}$ (FOPT).

The uncertainties entering the theoretical predictions are estimated below. The errors used and their impact on $R_{\tau,V/A}$ and $\alpha_s(M_\tau^2)$ are explicitly given in Table 5, while the total theoretical errors on $R_{\tau,V+A}$ and the moments are presented in Table 6. The correlation matrix of the theoretical errors between $R_{\tau,V+A}$ and the moments is given in Table 7.

– **Physical constants.** The relevant physical constants are
  (a) the CKM matrix element $|V_{ud}|$,
  (b) the electroweak radiative correction factor S_{EW},
  (c) the light quark masses m_u, m_d,
  (d) the quark condensates.

  Errors from the light quark masses are negligible while the others, in particular ΔS_{EW}, must be taken into account (see Table 5). For the quark condensates which contribute to dimension $D = 4$, the PCAC relation,

$$(m_u + m_d)\langle 0|\bar{u}u + \bar{d}d|0\rangle \simeq -2f_\pi^2 m_\pi^2 \ , \qquad (25)$$

  is used with the value for f_π given in Sect. 5. A theoretical uncertainty of 10% for the above relation is assumed.

– **Perturbative series.** The errors in the truncated perturbative expansion originate mainly from the unknown higher order expansion coefficient K_4. The authors of [50] advocate the principle of minimal sensitivity (PMS) [51], which allows the computation of a renormalization scheme (RS) with optimal convergence, i.e., with minimal dependence on higher order corrections. The difference between an observable calculated using the PMS and the $\overline{\mathrm{MS}}$ schemes can be used to provide an estimate of the missing terms accumulated in K_4. The procedure results in $K_4 \simeq 36$. In [52] an experimental estimate of K_4 is performed

Table 5. Sources of theoretical uncertainties and their impacts on $R_{\tau,V+A}$ and $\alpha_s(M_\tau^2)$ for $\alpha_s(M_\tau^2)=0.35$ and evolved to $\alpha_s(M_Z^2)$. The origins of the different errors are explained in the text. The effects on $R_{\tau,V/A}$ are one-half of $R_{\tau,V+A}$, while for V and A they are degenerate

Error source	Value $\pm\,\Delta^{\text{theo}}$	$\Delta^{\text{theo}} R_{\tau,V+A}$		$\Delta^{\text{theo}}\alpha_s(M_\tau^2)$		$\Delta^{\text{theo}}\alpha_s(M_Z^2)$	
		FOPT_{CI}	FOPT	FOPT_{CI}	FOPT	FOPT_{CI}	FOPT
S_{EW}	1.0194 ± 0.0040	0.014		0.006	0.004	0.0006	0.0004
V_{ud}	0.9752 ± 0.0007	0.005		0.002	0.001	0.0002	0.0001
K_4	50 ± 50	0.027	0.023	0.012	0.007	0.0013	0.0007
R-scheme (RS)	$\overline{\text{MS}} \to \text{PMS}$	0.022	0.035	0.010	0.010	0.0011	0.0011
R-scale μ	$M_\tau \to M_\tau \pm 0.7$	0.011	0.051	0.005	0.014	0.0005	0.0015
Total errors		0.039	0.068	0.018	0.019	0.0019	0.0020

Table 6. Total theoretical errors for the vector, axial-vector and $(V+A)$ ratios R_τ and the moments ($\alpha_s(M_\tau^2)=0.35$ assumed)

ALEPH	$\Delta^{\text{theo}} R_\tau$	$\Delta^{\text{theo}} D_\tau^{10}$	$\Delta^{\text{theo}} D_\tau^{11}$	$\Delta^{\text{theo}} D_\tau^{12}$	$\Delta^{\text{theo}} D_\tau^{13}$
$V_{\text{FOPT}_{\text{CI}}}$	0.019	0.0046	0.0038	0.0004	0.0003
$A_{\text{FOPT}_{\text{CI}}}$	0.019	0.0046	0.0033	0.0005	0.0003
$(V+A)_{\text{FOPT}_{\text{CI}}}$	0.039	0.0046	0.0035	0.0005	0.0003
$(V+A)_{\text{FOPT}}$	0.084	0.0094	0.0042	0.0020	0.0010

using the *a priori* freedom of the choice of the renormalization scale μ to increase the sensitivity of the perturbative series on K_4. This yields $K_4 = 27 \pm 5$. Motivated by the above and the expectation that the perturbative series for $\delta^{(0)}$ should have a constant sign behaviour with increasing coefficients [53], K_4 is chosen to be 50 ± 50.

Another important point is the renormalization scale (μ) dependence of the prediction expressed in the RGE which governs the running of α_s. Formally, the integrals (14) in (13) also obey the RGE [7]. In a truncated series the renormalization scale dependence remains and is therefore an intrinsic uncertainty of the theoretical prediction. In order to estimate its size, μ is varied from M_τ to $\mu = 1.1$ GeV and $\mu = 2.5$ GeV [7]. When changing the μ scale, the coefficients K_n of the perturbative expansion, as well as α_s, are reexpressed according to the RGE.

In addition to the renormalization scale dependence, the arbitrariness of the choice of the renormalization scheme leaves an ambiguity. Again an estimate of its associated uncertainty is obtained by changing the RS from $\overline{\text{MS}}$ to the PMS scheme. This transformation induces a reduction of $\alpha_s(M_\tau^2)$ of approximately 0.010 [55], which is taken as the corresponding uncertainty.

– **Nonperturbative operators.** The OPE power terms of dimensions $D = 4, 6, 8$ have no theoretical errors since they are free varying parameters of the fits and are therefore determined experimentally. Contributions from higher orders have not been calculated yet. However they can only contribute indirectly via a logarithmic dependence on s to R_τ. The operators of dimension $D = 10$ are then suppressed by $(\alpha_s/\pi)^2 / M_\tau^{10} \sim 4 \times 10^{-5}$, and thus neglected in this analysis. Also neglected is any non-standard dimension $D = 2$ term (except for the quark masses). Such terms are not generated by a dynamical QCD action and are therefore absent in the SVZ approach. However they are not ruled out experimentally and are still controversial theoretically [56]. No additional theoretical error is introduced to cover the possible existence of a $\delta^{(0)} \sim (\Lambda^2/s)$ term from the first ultraviolet singularity (renormalon) of the Borel resummed large-β_0 approximation of the perturbative series [9]. Any such uncertainty is assumed to be taken into account by the error ascribed to K_4.

Table 7. Correlations between $R_{\tau,V+A}$ and the moments from theoretical uncertainties using FOPT_{CI}

ALEPH	$R_{\tau,V+A}$	$D^{10}_{\tau,V+A}$	$D^{11}_{\tau,V+A}$	$D^{12}_{\tau,V+A}$	$D^{13}_{\tau,V+A}$
$R_{\tau,V+A}$	1	0.91	−0.89	−0.65	−0.85
$D^{10}_{\tau,V+A}$	–	1	−0.99	−0.63	−0.86
$D^{11}_{\tau,V+A}$	–	–	1	0.54	0.81
$D^{12}_{\tau,V+A}$	–	–	–	1	0.89
$D^{13}_{\tau,V+A}$	–	–	–	–	1

In [57–59], R_τ has been calculated employing a renormalon resummation of $\delta^{(0)}$ in the large-β_0 limit. The resummation is performed by evaluating the integral of the Borel transform in the large-β_0 limit, where infrared (IR) and ultraviolet (UV) singularities appear in the Borel plane. The UV renormalons, situated outside the integration range, have alternating signs and can be resummed.

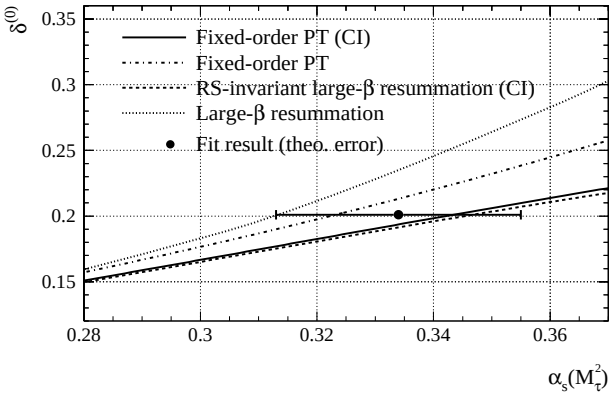

Fig. 12. Perturbative contribution $\delta^{(0)}$ to $R_{\tau,V/A}$ with different approaches. "CI" means contour-improved. The fixed-order PT curves are given for $K_4 = 50$. Both large-β_0 resummations are corrected for the first three, exactly known fixed-order coefficients. Also shown is the result (26) of this analysis within its estimated theoretical uncertainty

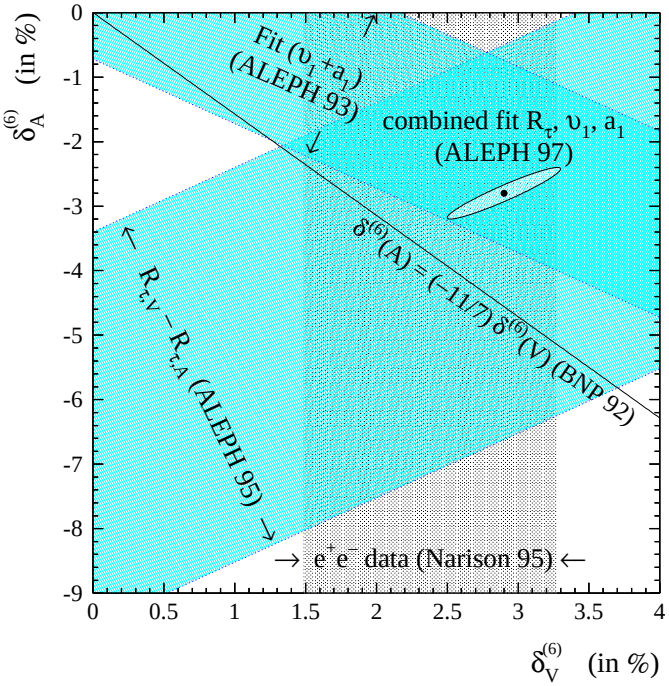

Fig. 13. Nonperturbative contributions $\delta_{V/A}^{(6)}$ to $R_{\tau,V/A}$. The ellipse depicts the new ALEPH result. The strong correlations of about 90% between $\delta_V^{(6)}$ and $\delta_A^{(6)}$ are found in an additional fit in which $R_{\tau,V}$ and $R_{\tau,A}$ and moments are combined. See Sect. 6.8.3 for a discussion of the precision shown here. The references are: "ALEPH 93" [2], "ALEPH 95" [26], "Narison 95" [61] and "BNP 92" [5]

However, the IR renormalons lie inside the integration range on the positive axis and give rise to nonperturbative power contributions which are absorbed in the OPE. The authors of [60] developed a RS-invariant all-orders renormalon resummation.

Figure 12 shows the results for $\delta^{(0)}$ using different methods to evaluate the perturbative series. The fixed-order PT corresponds to the Taylor expansion (15) and the contour-improved prediction is (13) with a numerical evaluation of the $A^{(n)}$ integrals. These procedures are applied here. The large-β_0 limit resummed perturbative prediction is taken from [58] and for the theoretical prediction of the RS-invariant large-β_0 resummed $\delta^{(0)}$ the formulae given in [60] are used. Both resummed predictions are corrected for the first three, exactly known fixed-order coefficients. Also shown is the fit result of this analysis with its estimated theoretical uncertainty. It covers the whole range of perturbative approaches presented above within one standard deviation.

6.7 Results of the fits

The fit minimizes the χ^2 of the differences between measured and fitted quantities contracted with the inverse of the sum of the experimental and theoretical covariance matrices taken from Tables 3 and 7.

The results are listed in Table 8. Table 9 gives the corresponding correlation matrices between the fitted parameters. The limited number of observables and the strong correlations between the spectral moments explain the large correlations observed, especially between the fitted nonperturbative operators. The precision of $\alpha_s(M_\tau^2)$ obtained with the two perturbative methods employed is comparable, however their central values differ by about 0.02 as seen in Fig. 12. The differences between $\mathrm{FOPT_{CI}}$ and FOPT for the nonperturbative parameters are negligible compared to their errors so that only the $\mathrm{FOPT_{CI}}$ values are given. The $\delta^{(2)}$ term is the pure theoretical contribution from the known masses of the light u, d quarks. No anomalous dimension $D = 2$ operator has been fitted since empirically it is found to be degenerate to α_s. The $\delta^{(4)}$ term receives contributions from the quark and gluon condensates and the quartic light quark masses. While the quark condensates and the quark masses are rather well known and are fixed theoretically by (25), the gluon condensate is adjusted in the fit.

One notices a remarkable agreement within statistical errors between the $\alpha_s(M_\tau^2)$ values using vector and axial-vector data. The results can be compared to the one obtained in the previous ALEPH analysis [2] where, applying $\mathrm{FOPT_{CI}}$, the strong coupling was measured to be $\alpha_s(M_\tau^2) = 0.330 \pm 0.046$ using the much smaller data set of 8500 τ decays.

The total nonperturbative power contribution to $R_{\tau,V+A}$ is compatible with zero within an uncertainty of 0.4%, that is much smaller than the error arising from the perturbative term. The advantage of separating the vector and axial-vector channels and comparing to the inclusive $(V + A)$ fit becomes obvious in the adjustment of the leading nonperturbative contributions of dimension $D = 6$ and $D = 8$, which cancel in the inclusive sum. This cancellation of the nonperturbative terms increases the confidence on the $\alpha_s(M_\tau^2)$ determination from the inclusive $(V + A)$ observables. The gluon condensate is fixed by the first $l = 0, 1$ moments which receive lowest order contributions while it is suppressed in R_τ by $(\alpha_s/\pi)^2$.

Table 8. Fit results of $\alpha_s(M_\tau^2)$ and the OPE nonperturbative contributions from vector, axial-vector and $(V + A)$ combined fits using the corresponding ratios R_τ and the spectral moments as input parameters. Where two errors are given they denote experimental (first number) and theoretical uncertainties (second number). The differences between $\mathrm{FOPT_{CI}}$ and FOPT for the nonperturbative parameters are negligible compared to their errors. The $\delta^{(2)}$ term is the pure theoretical prediction. The quark condensates in the $\delta^{(4)}$ term are fixed to their theoretical values, (25), and only the gluon condensate is varied as a free parameter. The total nonperturbative contribution is the sum $\delta_{\mathrm{NP}} = \delta^{(4)} + \ldots + \delta^{(8)}$

ALEPH	Vector (V)	Axial-Vector (A)	$V + A$
$\alpha_s(M_\tau^2)$ ($\mathrm{FOPT_{CI}}$)	$0.340 \pm 0.016 \pm 0.017$	$0.349 \pm 0.015 \pm 0.017$	$0.345 \pm 0.007 \pm 0.017$
$\alpha_s(M_\tau^2)$ (FOPT)	$0.320 \pm 0.012 \pm 0.019$	$0.328 \pm 0.011 \pm 0.019$	$0.322 \pm 0.005 \pm 0.019$
$\delta^{(0)}$ ($\mathrm{FOPT_{CI}}$)	0.198 ± 0.017	0.206 ± 0.018	0.202 ± 0.013
$\delta^{(0)}$ (FOPT)	0.197 ± 0.025	0.206 ± 0.026	0.200 ± 0.022
$\delta^{(2)}$	$-(0.3 \pm 0.3)\times 10^{-3}$	$-(0.6 \pm 0.3)\times 10^{-3}$	$-(0.4 \pm 0.2)\times 10^{-3}$
$\delta^{(4)}$	$(0.6 \pm 0.8)\times 10^{-3}$	$(-5.7 \pm 0.9)\times 10^{-3}$	$-(2.5 \pm 0.8)\times 10^{-3}$
$\delta^{(6)}$	0.029 ± 0.004	-0.029 ± 0.004	0.001 ± 0.004
$\delta^{(8)}$	-0.009 ± 0.001	0.008 ± 0.001	-0.001 ± 0.001
Total δ_{NP}	0.020 ± 0.004	-0.027 ± 0.004	-0.003 ± 0.004
χ^2/d.o.f.	0.1/1	0.1/1	0.2/1

Table 9. Correlation matrices according to the fits presented in Table 8 for vector (left table), axial-vector (middle) and $(V + A)$ (right table) using $\mathrm{FOPT_{CI}}$. As the gluon condensate contributes only insignificantly to $\delta^{(4)}$, the correlations to the total $\delta^{(4)}$ term are tiny

ALEPH	$\langle GG\rangle_V$	$\delta_V^{(6)}$	$\delta_V^{(8)}$	$\langle GG\rangle_A$	$\delta_A^{(6)}$	$\delta_A^{(8)}$	$\langle GG\rangle_{V+A}$	$\delta_{V+A}^{(6)}$	$\delta_{V+A}^{(8)}$
$\alpha_s(M_\tau^2)$	-0.24	-0.18	-0.11	-0.47	0.38	-0.38	0.14	-0.01	0.13
$\langle GG\rangle_{V/A/V+A}$	1	0.78	0.82	1	-0.85	0.90	1	-0.68	0.78
$\delta^{(6)}_{V/A/V+A}$	–	1	-0.98	–	1	-0.98	–	1	-0.95
$\delta^{(8)}_{V/A/V+A}$	–	–	1	–	–	1	–	–	1

Taking the value obtained in the $(V + A)$ inclusive fit and adding as systematic uncertainties half of the difference between the vector and axial-vector fits as well as the $\mathrm{FOPT_{CI}}$ and FOPT results, the gluon condensate is found to be $\langle(\alpha_s/\pi)GG\rangle = (0.001 \pm 0.015)\ \mathrm{GeV}^4$. An interesting observation is the alternating sign in both vector and axial-vector cases between the $\delta^{(6)}$ and $\delta^{(8)}$ terms. This is connected with the special form of the shape of $R_{\tau,V}(s_0)$ ($R_{\tau,A}(s_0)$) as a function of a varying "τ mass" $s_0 \le M_\tau^2$, as will be discussed in the following section. Figure 13 shows the measured $\delta_A^{(6)}$ versus $\delta_V^{(6)}$ in comparison with other estimations of both experimental and theoretical origin.

In order to check the consistency of the different approaches one can use either the normalization, i.e., the ratio R_τ obtained from the hadronic branching ratios, or the explicit form of the spectral functions, i.e., the spectral moments. The value of $\alpha_s(M_\tau^2)$ can then be determined using variables coming from only one of these inputs. This is done for the $(V + A)$ case for which contributions from nonperturbative terms are small, so that the effect of additional theoretical assumptions are minimized. The results of these fits using $\mathrm{FOPT_{CI}}$ are shown in Fig. 14.

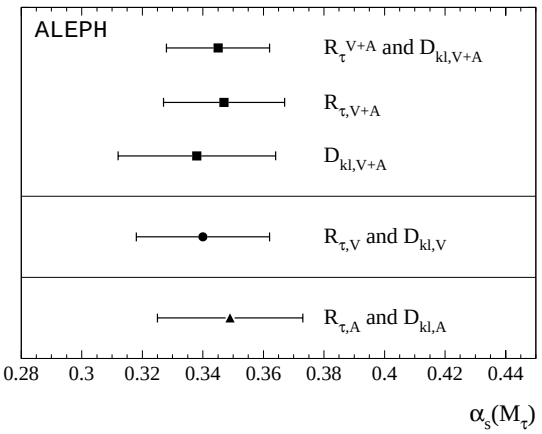

Fig. 14. Results for $\alpha_s(M_\tau^2)$ using $R_{\tau,V+A}$ only, the moments D_{V+A}^{kl} only and the combined information from vector and axial-vector τ decays using $\mathrm{FOPT_{CI}}$. The measurements are strongly correlated due to the dominant theoretical errors

As mentioned in the introduction, there exists no constraining prescription which allows a resolution of the am-

biguity between $\mathrm{FOPT_{CI}}$ and FOPT. The final result on $\alpha_s(M_\tau^2)$ is thus the average of the two values given in Table 8, with half of their difference added as theoretical error. The evolution of the $\alpha_s(M_\tau^2)$ measurement from the inclusive $(V+A)$ observables based on the Runge-Kutta integration of the differential equation to $\mathrm{N^3LO}$ [44,64, 65,62,66] yields

$$\begin{aligned} \alpha_s(M_\tau^2) &= 0.334 \pm 0.007_{\mathrm{exp}} \pm 0.021_{\mathrm{theo}} \\ \alpha_s(M_Z^2) &= 0.1202 \pm 0.0008_{\mathrm{exp}} \pm 0.0024_{\mathrm{theo}} \\ &\quad \pm 0.0010_{\mathrm{evol}} \end{aligned} \tag{26}$$

The first error accounts for the experimental uncertainty, the second number gives the uncertainty of the theoretical prediction of R_τ and the spectral moments as well as the ambiguity of the theoretical approaches employed, and the last error stands for possible ambiguities in the evolution due to uncertainties in the matching scales of the quark thresholds [66]. Effects associated with the truncation of the RGE at $\mathcal{O}(\alpha_s^5)$ are small: the new $\mathrm{N^3LO}$ order [44] gives a tiny contribution of $\alpha_s(M_Z^2)_{3-\mathrm{loop}} - \alpha_s(M_Z^2)_{4-\mathrm{loop}} = 0.0003$.

The results (26) are obtained using the world average value for the leptonic branching ratio (3). Employing only ALEPH measurements [13,63] one obtains $B(\tau^- \to e^-\,\bar{\nu}_e\nu_\tau) = (17.785 \pm 0.069)\%$ resulting in $\alpha_s(M_\tau^2) = 0.335 \pm 0.011_{\mathrm{exp}} \pm 0.021_{\mathrm{theo}}$. The evolution to the Z boson mass yields $\alpha_s(M_Z^2) = 0.1204 \pm 0.0013_{\mathrm{exp}} \pm 0.0024_{\mathrm{theo}} \pm 0.0010_{\mathrm{evol}}$.

One can express the value of $\alpha_s(M_\tau^2)$ in terms of the $\overline{\mathrm{MS}}$ renormalization scale $\Lambda_{\overline{\mathrm{MS}}}$ at four loop level. For the result (26) with three active flavours one has

$$\Lambda_{\overline{\mathrm{MS}}}^{(3)} = (370 \pm 13_{\mathrm{exp}} \pm 38_{\mathrm{theo}})\ \mathrm{MeV}\ . \tag{27}$$

6.8 Test of the running of $\alpha_s(s)$ at low energies

The analysis presented in the preceeding section indicates that the framework of the perturbative expansion and the OPE approach, used for the theoretical prediction of the measured quantities, describes data phenomenologically. The exclusive measurement of the vector and axial-vector spectral functions allows further investigations of QCD phenomena at low energies up to the τ mass.

6.8.1 Running using a hypothetical τ mass

Using the spectral functions, one can simulate the physics of a hypothetical τ lepton with a mass $\sqrt{s_0}$ smaller than M_τ through (10). Assuming quark-hadron duality, the evolution of $R_\tau(s_0)$ provides a direct test of the running of $\alpha_s(s_0)$, governed by the RGE β-function. On the other hand, it is a test of the validity of the OPE approach in τ decays. The studies performed in this section employ

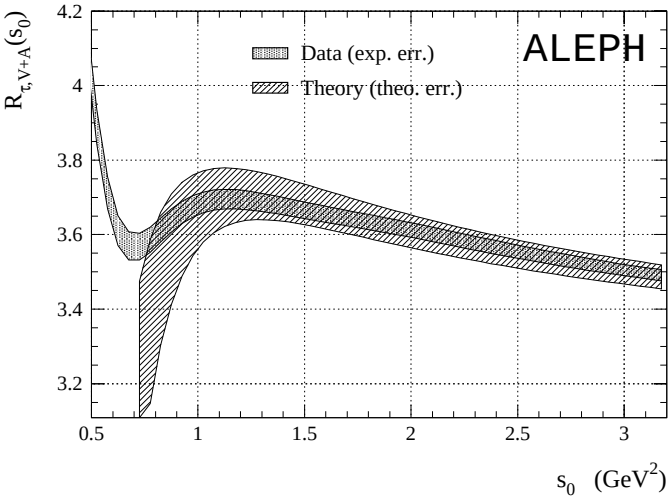

Fig. 15. The ratio $R_{\tau,V+A}$ versus the square "τ mass" s_0. The curves are plotted as error bands to emphasize their strong point-to-point correlations in s_0. Also shown is the theoretical prediction using $\mathrm{FOPT_{CI}}$ and the results for $R_{\tau,V+A}$ and the nonperturbative terms from Table 8. The theoretical errors are taken from Table 5

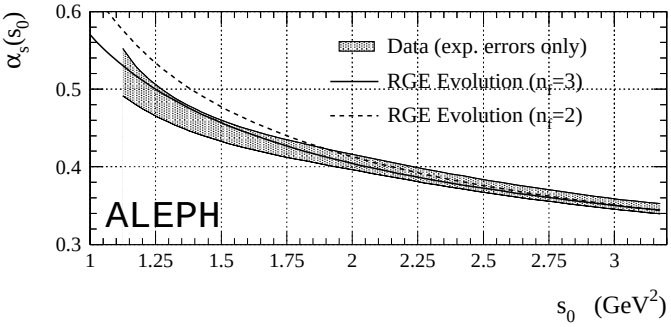

Fig. 16. The running of $\alpha_s(s_0)$ obtained from the fit of the theoretical prediction to $R_{\tau,V+A}(s_0)$. The shaded band shows the data including experimental errors. The curves give the four-loop RGE evolution for two and three flavours

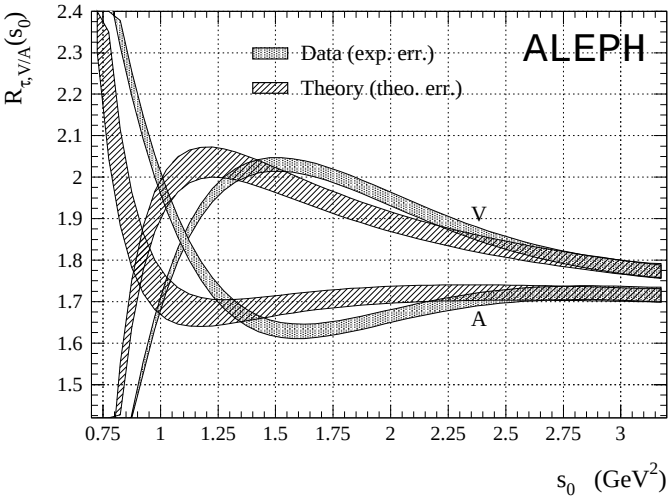

Fig. 17. The ratios $R_{\tau,V}$ and $R_{\tau,A}$ versus the square "τ mass" s_0 for data and the theoretical prediction using the results of Table 8

only $\mathrm{FOPT_{CI}}$. Results obtained with FOPT are similar and differ only in the central $\alpha_s(M_\tau^2)$ value.

The functional dependence of $R_{\tau,V+A}(s_0)$ is plotted in Fig. 15 together with the theoretical prediction using the results of Table 8. The spread due to uncertainties are shown as bands. In the $(V+A)$ case, the experimental errors are diminished by normalizing $R_{\tau,V+A}(s_0 = M_\tau^2)$ to (22). The correlations between two adjacent bins $s_1 < s_2$ are large as the only new information is provided by the small mass difference between the two bins and the slightly different weight function. They are reinforced by the original experimental and theoretical correlations. Below 1 GeV^2 the error of the theoretical prediction of $R_{\tau,V+A}(s_0)$ starts to blow up due to the increasing uncertainty from the unknown K_4 perturbative term; errors of the nonperturbative contributions are *not* contained in the theoretical error band. Figure 16 shows the plot corresponding to Fig. 15, translated into the running of $\alpha_s(s_0)$, i.e., the experimental value for $\alpha_s(s_0)$ has been individually determined at every s_0 from the comparison of data and theory. Also plotted is the four-loop RGE evolution using two and three quark flavours.

Figure 17 gives the vector and axial-vector ratios $R_{\tau,V/A}$ as a function of s_0 together with the corresponding theoretical predictions using as input the fitted parameters of Table 8. By construction data and theory converge at M_τ^2, but the observed agreement is much less stable than in the $(V+A)$ case. As a consequence one might question the reliability of the OPE approach at the scale M_τ^2 for vector or axial-vector only. On the other hand, the agreement of the $\alpha_s(M_\tau^2)$ values for V and A (see Table 8) may indicate that within the achieved precision, nonperturbative contributions are well absorbed by the dimension $D = 6, 8$ power terms. Nevertheless, the deviation between data and theory observed implies that the values of the fitted parameters should depend on the spectral moments used, i.e., of the specific shape of the weighting function inserted in the integral (16). These systematic uncertainties are quantified in Sect. 6.8.3.

The experimental fact that the nonperturbative contributions cancel over the whole range $1.2\ \mathrm{GeV}^2 \le s_0 \le M_\tau^2$ leads to confidence that the α_s determination from the inclusive $(V+A)$ data is robust.

6.8.2 Running via the integration range

Another definition of the evolution of $R_\tau(s_0)$, which will be denoted $\tilde{R}_\tau(s_0)$, is obtained by varying only the integration range of (10) for $s_0 < M_\tau^2$ whilst keeping $s_0 = M_\tau^2$ in the integrand. This evolution technique differs intrinsically from the one applied in the previous section by the choice of the weight function under the integral. It was originally proposed in [6] and has been applied to data in [67]. The integrals $A^{(n)}(\alpha_s)$ used in (13) to calculate the contribution from perturbation theory become

$$\tilde{A}^{(n)}(\alpha_s) = \frac{1}{2\pi i} \oint\limits_{|s|=s_0} \frac{ds}{s} \left[\frac{2(s_0 - s)}{M_\tau^2} - \frac{2(s_0^3 - s^3)}{M_\tau^6} + \frac{s_0^4 - s^4}{M_\tau^8} \right] \left(\frac{\alpha_s(-s)}{\pi} \right)^n . \quad (28)$$

In contrast to (12), in which the relative importance of the dimensional OPE terms increases when decreasing s_0, here the nonperturbative contribution remains constant, i.e., a series in powers of M_τ^{-D} [6]. This property amplifies the sensitivity of the observable to the perturbative part assuming validity of the OPE expansion down to s_0. However, for integration ranges $s_0 < M_\tau^2$ the above defined integrand does not suppress the correlation function on the real axis and as a consequence the OPE might not be well behaved [4,5]. Figure 18 shows the data distribution (with error band) of $\tilde{R}_{\tau,V+A}(s_0)$ together with the various theoretical predictions (upper plot) and the ratios of data and theory (lower plot). The experimental errors were again diminished by normalizing $\tilde{R}_{\tau,V+A}(s_0 = M_\tau^2)$ to (22). The theoretical errors are given representatively for the $\mathrm{FOPT_{CI}}$ prediction. Included in the theoretical errors is an s_0-independent error of 0.4% for the nonperturbative prediction. The RS-invariant and RS-dependent large-β_0 resummation results are obtained using the formulae given in [60] and [58], respectively. The adjusted $\alpha_s(M_\tau^2)$ values which fit the theoretical predictions of $\tilde{R}_{\tau,V+A}(M_\tau^2)$ to the data are: 0.345 (0.322) for the $\mathrm{FOPT_{CI}}$ (FOPT) approach, see Table 8, and 0.349 (0.302) for the RS-invariant (RS-dependent[2]) large-β_0 resummation. One notices the improved convergence of the contour-improved perturbation theories compared to the FOPT expansion that blows up at $s_0 < 0.5\ \mathrm{GeV}^2$ (Fig. 18). All theoretical approaches with a contour-improved calculation of the complex integral have a similar shape and differ only in the total normalization, i.e., $\alpha_s(M_\tau^2)$. Using the known FOPT expansion coefficients up to order α_s^3 and adding the coefficients obtained from the large-β_0 resummation [58] gives qualitatively a similar curve as the truncated FOPT expansion result, again with a different normalization [67].

The good agreement of $\mathrm{FOPT_{CI}}$ for $s_0 > 0.8\ \mathrm{GeV}^2$ observed in Fig. 15 can be understood to be due to the additional dependence of the nonperturbative contributions on s_0. The shortcomings of the perturbative prediction at small energy is covered by the additional nonperturbative degrees of freedom. The latter are not operational for $\tilde{R}_{\tau,V+A}(s_0)$, although the s_0 behaviour postulated by the OPE is still assumed down to the smallest s_0 values.

6.8.3 Systematic uncertainties from the OPE approach

The tests of the running of $R_{\tau,V/A}(s_0)$ performed in the previous sections revealed inconsistencies between data and theory for the vector and axial-vector cases. Deviations from the SVZ approach within the parametrization of [5] introduce systematic uncertainties into the determination of α_s and the non-perturbative power corrections.

[2] The value of 0.302 for the large-β_0 resummation differs from Fig. 12 since the latter has been corrected for the first three exactly known fixed-order coefficients. The corrected value reads $\alpha_s(M_\tau^2) = 0.313$

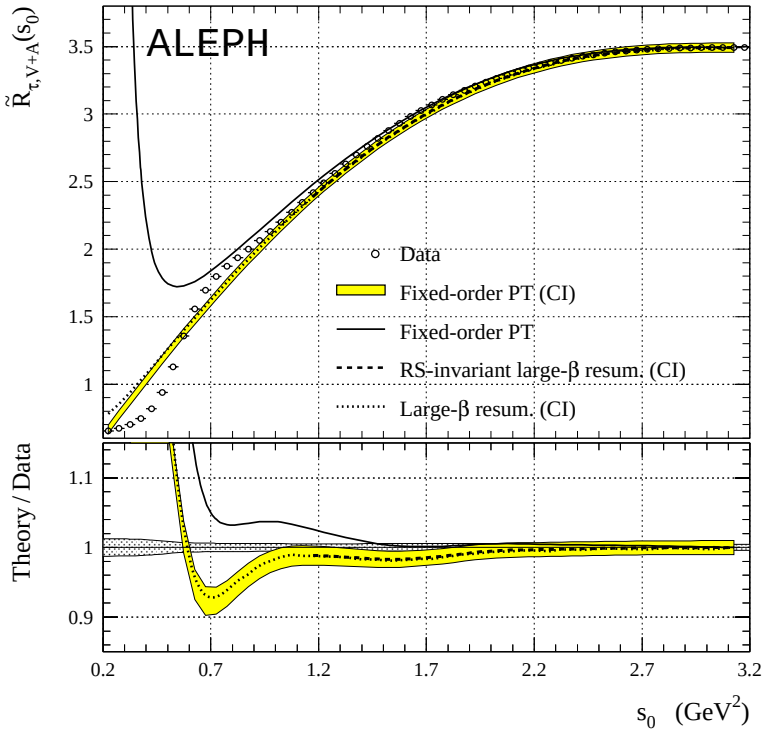

Fig. 18. $\tilde{R}_{\tau,V+A}$ versus the integration range s_0. The hollow points depict the data distribution, while the shaded band shows the $\mathrm{FOPT_{CI}}$ prediction with theoretical errors. The solid line gives the FOPT expansion (15). Represented by the dashed line is the RS-invariant, improved large-β_0 resummation technique of [60] and the dotted line gives the large-β_0 resummation of [58]. The lower plot shows the ratio of the theoretical predictions to the data where the dotted horizontal band shows the uncertainties on the data points

Table 10. Systematic uncertainties due to deviations from the OPE parametrization of [5]

	V	A	V+A
$\Delta\alpha_s(M_\tau^2)$	0.022	0.012	0.004
$\Delta\delta^{(6)}$	0.016	0.008	0.002
$\Delta\delta^{(8)}$	0.004	0.003	0.001

The amount of those effects can be evaluated by varying the fit procedure used to determine Table 8. Fitting directly the $R_{\tau,V/A/V+A}$ curves shown in Figs. 15 and 17, for energies between 0.8 $\mathrm{GeV}^2 \le s_0 \le M_\tau^2$ for $(V+A)$ and 1.9 $\mathrm{GeV}^2 \le s_0 \le M_\tau^2$ for V/A, to the OPE improves the agreement between data and theory in these limited energy intervals while it becomes worse at lower s_0. Table 10 gives the systematic uncertainties due to the deviations of the adjusted parameters from the results of Table 8. The uncertainties on the vector and axial-vector nonperturbative contributions found here are much larger than the experimental and theoretical errors of the fit values (Table 8). After adding these systematic uncertainties, the total nonperturbative contributions become

$$\delta_{\mathrm{NP},V} = 0.020 \pm 0.017 \ , \tag{29}$$

$$\delta_{\mathrm{NP},A} = -0.027 \pm 0.009 \ , \tag{30}$$

$$\delta_{\mathrm{NP},V+A} = -0.003 \pm 0.005 \ . \tag{31}$$

The good agreement between data and theory found for the running of $R_{\tau,V+A}(s_0)$ (Fig. 15) contributes negligible uncertainties to the $(V+A)$ fit errors of Table 8.

6.8.4 Direct test of the nonperturbative prediction

To test whether the $D=6$ and $D=8$ terms of the OPE represent genuine nonperturbative contributions arising in $R_{\tau,V}(s_0)$ and $R_{\tau,A}(s_0)$, one can use $R_{\tau,V-A}(s_0)$ which is independent of the perturbative contribution to all orders in perturbation theory. Figure 19 shows $R_{\tau,V-A}$ versus the hypothetical τ mass $\sqrt{s_0}$. There is a positive remnant of about two standard deviations at M_τ^2 and the range of validity for the OPE, the latter shown by the dashed line in Fig. 19, has become smaller. The disagreement between data and theory at energies below 2.5 GeV^2 may be due to an intrinsic problem of the SVZ approach. On the other hand it could be generated by deviations of the dimension $D=6$ contribution from the vacuum saturation hypothesis adopted in [5]. Accounting for the neglected logarithmic s dependence of the $D=6$ and $D=8$ Wilson coefficients may improve the theoretical prediction.

It is instructive to perform a fit with a single power term,

$$R_{\tau,V-A}(s_0) = \frac{3}{2}|V_{ud}|^2 S_{\mathrm{EW}} \left(\frac{C_D\langle\mathcal{O}_D\rangle}{s_0^{D/2}} \right) \ , \tag{32}$$

for the interval 2 $\mathrm{GeV}^2 \le s_0 \le M_\tau^2$ with the dimension D and the term $C_D\langle\mathcal{O}_D\rangle$ as free parameters. The results are

$$\begin{aligned} D &= 6.9 \ \pm \ 0.9 \\ C_D\langle\mathcal{O}_D\rangle &= 2.3 \ \pm \ 0.7 \ , \end{aligned} \tag{33}$$

with an anti-correlation of 97% between the fitted quantities. This supports the conjecture [4,5] of a dominant power of dimension $D=6$.

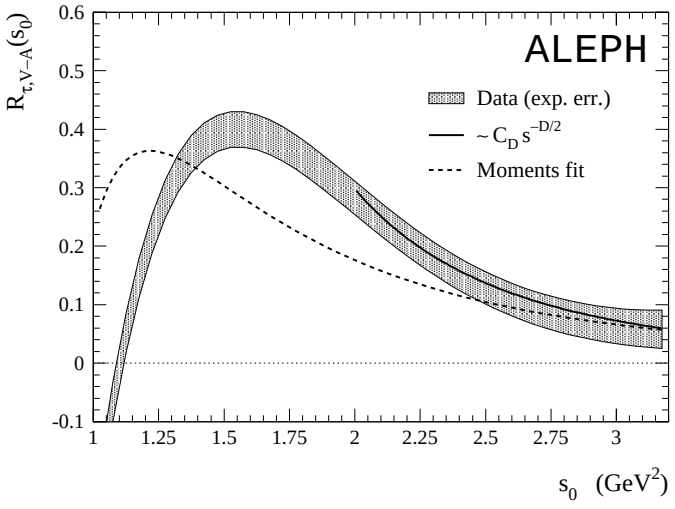

Fig. 19. Difference of vector and axial-vector ratios $R_{\tau,V-A}$ versus the "τ mass" s_0. The solid line corresponds to the fit (32, 33), while the dashed line shows the results of Table 8 obtained with the moments fit

7 Conclusions

Measurements are presented of the non-strange τ vector and axial-vector current hadronic spectral functions as well as their inclusive sum and difference. The distributions and corresponding error matrices can be obtained as postscript and data files from the ALEPH publication server on the WWW[3].

The separation of vector and axial-vector spectral functions allows to test chiral sum rules up to the τ mass.

The spectral functions and measurements of the ratios $R_{\tau,V/A/V+A}$ of the vector and axial-vector hadronic widths and the electronic width are exploited in order to obtain a precise determination of the strong coupling constant $\alpha_s(M_\tau^2)$. Since QCD is applied at a low energy scale, nonperturbative effects are accounted for by the use of the Operator Product Expansion (OPE), with coefficients which can be fitted simultaneously with $\alpha_s(M_\tau^2)$.

The best and most robust determination of $\alpha_s(M_\tau^2)$ is obtained from the inclusive $(V+A)$ fit. Using the world averages for the τ leptonic branching ratios and the τ lifetime to obtain R_τ yields $\alpha_s(M_\tau^2) = 0.334 \pm 0.007 \pm 0.021$, where the first error accounts for experimental and the second for theoretical uncertainties. The result is the mean value of those obtained using fixed-order perturbation theory (FOPT) and contour-improved FOPT. Evolving the above value from the τ to the Z mass scale gives $\alpha_s(M_Z^2) = 0.1202 \pm 0.0008 \pm 0.0024 \pm 0.0010$, where the last number gives the evolution uncertainty. The total nonperturbative contribution to $R_{\tau,V+A}$ is found to be compatible with zero. However, the same fit using the exclusive vector and axial-vector ratio $R_{\tau,V/A}$ and moments revealed that the nonperturbative contributions, in particular of dimension $D = 6$, are large, but almost exactly cancel out in the inclusive sum.

[3] http://alephwww.cern.ch/ALPUB/paper/paper.html

The spectral function measurement allows the possibility to derive R_τ as a function of a variable "τ mass" $s_0 \leq M_\tau^2$, taking advantage of the universal nature of the measured spectral functions. This provides a direct test of the running of $\alpha_s(s_0)$ which governs the evolution of the theoretical prediction to values smaller than the τ mass. Excellent agreement between the measured $R_{\tau,V+A}(s_0)$ and theory is found for the range of 0.8 GeV$^2 \leq s_0 \leq M_\tau^2$, below which $R_{\tau,V+A}(s_0)$ starts to diverge due to the influence of the ρ peak and the pion pole.

The evolution of the nonperturbative contributions as a function of s_0 can be accessed directly by considering $R_{\tau,V-A}(s_0)$ in which perturbative contributions cancel. The fit of one operator with variable dimension to $R_{\tau,V-A}(s_0)$ yields $D = 6.9 \pm 0.9$, in agreement with the assumption of a dominant $D = 6$ contribution made in the SVZ approach.

Acknowledgements. We gratefully acknowledge our colleagues from the accelerator divisions for the successful operation of LEP. We are indebted to the engineers and technicians in all our institutions for their contribution to the excellent performance of ALEPH. Those of us from non-member countries thank CERN for its hospitality. We are indebted to G. Altarelli, M. Beneke, S. Eidelman, G. Grunberg, S. Narison, P. Nason, M. Neubert, P.A. Rączka, A. Vainshtein, for a useful and very interesting one-day-long discussion. Comments from A. Kataev are also acknowledged. Special thanks to C.J. Maxwell, S. Menke, A. Pich and D.G. Tonge for the continuous theoretical and technical support.

Appendix

Table 1 lists the vector and axial-vector τ final states and the corresponding branching ratios. The following modes containing kaons are used as input into the sum of all τ branching ratios normalized to one and for the experimental subtraction of the Cabibbo suppressed modes. The numbers are mainly taken from [48,11]. Some are obtained from isospin considerations (see Sect. 4):

$B(\tau^- \to \mathrm{K}^- \nu_\tau)$	=	$(0.69 \pm 0.03)\%$
$B(\tau^- \to \mathrm{K}^* \nu_\tau)$	=	$(1.27 \pm 0.09)\%$
$B(\tau^- \to \mathrm{K}^- 2\pi^0 \nu_\tau)$	=	$(0.09 \pm 0.02)\%$
$B(\tau^- \to \mathrm{K}^- \pi^+ \pi^- \nu_\tau)$	=	$(0.23 \pm 0.05)\%$
$B(\tau^- \to \mathrm{K}^0 \pi^- \pi^0 \nu_\tau)$	=	$(0.35 \pm 0.08)\%$
$B(\tau^- \to \mathrm{K}^- \pi^- \pi^+ \pi^0 \nu_\tau)$	=	$(0.07 \pm 0.05)\%$
$B(\tau^- \to \mathrm{K}^- \mathrm{K}^0 \nu_\tau)$	=	$(0.19 \pm 0.04)\%$
$B(\tau^- \to \mathrm{K}^- \mathrm{K}^+ \pi^- \nu_\tau)$	=	$(0.16 \pm 0.03)\%$
$B(\tau^- \to \mathrm{K}^0 \bar{\mathrm{K}}^0 \pi^- \nu_\tau)$	=	$(0.16 \pm 0.03)\%$
$B(\tau^- \to \mathrm{K}^- \mathrm{K}^0 \pi^0 \nu_\tau)$	=	$(0.10 \pm 0.05)\%$
$B(\tau^- \to \mathrm{K}\bar{\mathrm{K}}\pi\pi \nu_\tau)$	=	$0.16\,\%$ (estimated)

References

1. R. Barate et al. (ALEPH Collaboration), Z. Phys. **C76** (1997) 15
2. D. Buskulic et al. (ALEPH Collaboration), Phys. Lett. **B307** (1993) 209
3. T. Coan et al. (CLEO Collaboration), Phys. Lett. **B356** (1995) 580

4. M.A. Shifman, A.L. Vainshtein and V.I. Zakharov, Nucl. Phys. **B147** (1979) 385, 448, 519
5. E. Braaten, S. Narison and A. Pich, Nucl. Phys. **B373** (1992) 581
6. F. Le Diberder and A. Pich, Phys. Lett. **B289** (1992) 165
7. F. Le Diberder and A. Pich, Phys. Lett. **B286** (1992) 147
8. A. Pich, Nucl. Phys. **B39** (Proc. Suppl.) (1995) 326
9. G. Altarelli, P. Nason and G. Ridolfi, Z. Phys. **C68** (1995) 257
10. S. Narison, Nucl. Phys. **B40** (Proc. Suppl.) (1995) 47; P.A. Rączka and A. Szymacha, Z. Phys. **C70** (1996) 125
11. R.M. Barnett et al. (Particle Data Group) Phys. Rev. **D54** (1996) 1
12. W. Marciano and A. Sirlin, Phys. Rev. Lett. **61** (1988) 1815; Phys. Rev. Lett. **61** (1986) 1815
13. D. Buskulic et al. (ALEPH Collaboration), Z. Phys. **C70** (1996) 561
14. A. Anastassov et al. (CLEO Collaboration), Phys. Rev. **D55** (1997) 2559; P. Abreu et al. (DELPHI Collaboration), Phys. Lett. **B355** (1995) 415; R. Akers et al. (OPAL Collaboration), Phys. Lett. **B369** (1996) 163; Z. Phys. **C67** (1995) 543
15. D. Buskulic et al. (ALEPH Collaboration), Report CERN PPE/97-090 (1997); R. Balest et al. (CLEO Collaboration), Phys. Lett. **388** (1996) 402; P. Abreu, (DELPHI Collaboration), Phys. Lett. **B365** (1996) 448; M. Acciarri et al. (L3 Collaboration), Phys. Lett. **B389** (1996) 187; R. Akers, (OPAL Collaboration), Phys. Lett. **B374** (1996) 341
16. R. Alemany, M. Davier and A. Höcker, Report LAL 97-02 (1997)
17. J.Z. Bai et al. (BES Collaboration), Phys. Rev. **D53** (1996) 20
18. D. Decamp et al. (ALEPH Collaboration), Nucl. Inst. Meth. **A294** (1990) 121
19. D. Buskulic et al. (ALEPH Collaboration), Nucl. Inst. Meth. **A360** (1995) 481
20. S. Jadach, J.H. Kühn and Z. Wąs, Comp. Phys. Comm. **64** (1991) 275
21. S. Jadach, B.F.L. Ward and Z. Wąs, Comp. Phys. Comm. **79** (1994) 503
22. S. Jadach et al., Comp. Phys. Comm. **76** (1993) 361
23. R. Brun et al., GEANT3.15, Report CERN DD/EE/84-1 (1984)
24. A. Höcker, "Measurement of the τ spectral functions and applications to QCD", Thesis, Report LAL 97-18, Orsay, France (1997)
25. D. Buskulic et al. (ALEPH Collaboration), Z. Phys. **C62** (1994) 539
26. D. Buskulic et al. (ALEPH Collaboration), Z. Phys. **C70** (1996) 579
27. D. Decamp et al. (ALEPH Collaboration), Z. Phys. **C54** (1992) 211
28. A. Höcker and V. Kartvelishvili, Nucl. Inst. Meth. **A372** (1996) 469
29. D. Buskulic et al. (ALEPH Collaboration), Z. Phys. **C74** (1997) 263
30. P.L. Campana, Nucl. Phys. **B55 C** (Proc. Suppl.) (1997) 161
31. V. Shelkov, Nucl. Phys. **B55 C** (Proc. Suppl.) (1997) 195
32. T. Das, V.S. Mathur and S. Okubo, Phys. Rev. Lett. **19** (1967) 895
33. S.R. Amendolia et al. (NA7 Collaboration), Nucl. Phys. **B277** (1986) 168
34. S. Weinberg, Phys. Rev. Lett. **18** (1967) 507.
35. T. Das, G.S. Guralnik, V.S. Mathur, F.E. Low and J.E. Young, Phys. Rev. Lett. **18** (1967) 759
36. J.F. Donoghue and E. Golowich, Phys. Rev. **D49** (1994) 1513
37. L.R. Surguladze and M.A. Samuel, Phys. Rev. Lett. **66** (1991) 560; S.G. Gorishny, A.L. Kataev and S.A. Larin, Phys. Lett. **B259** (1991) 144
38. J.H. Kühn and A. Santamaria, Z. Phys. **C48** (1990) 445
39. A. Pais, Ann. Phys. **9** (1960) 548
40. E. Braaten, Phys. Rev. Lett./ **60** (1988) 1606
41. E. Braaten and C.S. Li, Phys. Rev. **D42** (1990) 3888
42. K.G. Wilson, Phys. Rev. **179** (1969) 1499
43. K.G. Chetyrkin and A. Kwiatkowski, Z. Phys. **C59** (1993) 525
44. S.A. Larin, T. van Ritbergen and J.A.M. Vermaseren, Phys. Lett. **B400** (1997) 379
45. A.A. Pivovarov, Sov. J. Nucl. Phys. **54** (1991) 676, Z. Phys. **C53** (1992) 461
46. C. Becchi, S. Narison, E. de Rafael and F.J. Yndurain, Z. Phys. **C8** (1981) 335; D.J. Broadhurst, Phys. Lett. **B101** (1981) 423; S.C. Generalis, J. Phys. **G15** (1989) L225
47. D.J. Broadhurst and S.C. Generalis, Phys. Lett. **165** (1985) 175
48. M. Davier, Nucl. Phys. **B55 C** (Proc. Suppl.) (1997) 395
49. S. Chen (ALEPH Collaboration), Talk given at the High-Energy Physics International Euroconference on Quantum Chromodynamics (QCD 97), Montpellier, France 1997
50. A.L. Kataev, V.V. Starshenko, Mod. Phys. Lett. **A10** (1995) 235; Nucl. Phys. **B39** (Proc. Suppl.) (1995) 312
51. P.M. Stevenson, Phys. Rev. **D23** (1981) 2916
52. F. Le Diberder, Nucl. Phys. **B39** (Proc. Suppl.) (1995) 318
53. A.L. Kataev, private communication (1997)
54. G. Grunberg, Phys. Lett. **B95** (1980) 70; Phys. Rev. **D29** (1984) 2315
55. P.A. Rączka, Report DTP/97/50 (1997)
56. G. Grunberg, Report CPTH-PC510-0597 (1997)
57. M. Beneke and V.M. Braun, Phys. Lett. **B348** (1995) 513; P. Ball, M. Beneke and V.M. Braun, Nucl. Phys. **B452** (1995) 563.
58. M. Neubert, Report CERN-TH-7524-94 (1994); Nucl. Phys. **B463** (1996) 511
59. C.N. Lovett-Turner and C.J. Maxwell, Nucl. Phys. **B452** (1995) 188
60. C.J. Maxwell and D.G. Tonge, Nucl. Phys. **B481** (1996); Report DTP-97-30 (1997)
61. S. Narison, Phys. Lett. **B361** (1995) 121
62. W. Bernreuther, W. Wetzel, Nucl. Phys. **B197** (1982) 228; W. Wetzel, Nucl. Phys. **B196** (1982) 259; W. Bernreuther, Talk given at the Workshop on QCD at LEP, Aachen, Germany 1994, PITHA-94-31 (1994)
63. R. Barate et al. (ALEPH Collaboration), Report CERN PPE/97-090 (1997)
64. K.G. Chetyrkin, B.A. Kniehl and M. Steinhauser, Phys. Rev. Lett. **79** (1997) 2184
65. K.G. Chetyrkin, B.A. Kniehl and M. Steinhauser, Nucl. Phys. **B510** (1998) 61
66. G. Rodrigo, A. Pich, A. Santamaria, FTUV-97-80 (1997)
67. M. Girone and M. Neubert, Phys. Rev. Lett. **76** (1996) 3061